Eur. Phys. J. E (2023) 46:107
https://doi.org/10.1140/epje/s10189-023-00363-x

THE EUROPEAN PHYSICAL JOURNAL E

Regular Article – Soft Matter

Effect of ionic strength on the assembly of simian vacuolating virus capsid protein around poly(styrene sulfonate)

Roi Asor[1,a], Surendra W. Singaram[2,b], Yael Levi-Kalisman[3,c], Michael F. Hagan[2,d], and Uri Raviv[1,e]

[1] Institute of Chemistry and the Center for Nanoscience and Nanotechnology, The Hebrew University of Jerusalem, Edmond J. Safra Campus, Givat Ram, 9190401 Jerusalem, Israel
[2] Department of Physics, Brandeis University, 415 South Street, Waltham 02453, MA, USA
[3] Institute of Life Sciences and the Center for Nanoscience and Nanotechnology, The Hebrew University of Jerusalem, Edmond J. Safra Campus, Givat Ram, 9190401 Jerusalem, Israel

Received 13 June 2023 / Accepted 9 October 2023 / Published online 2 November 2023

Abstract Virus-like particles (VLPs) are noninfectious nanocapsules that can be used for drug delivery or vaccine applications. VLPs can be assembled from virus capsid proteins around a condensing agent, such as RNA, DNA, or a charged polymer. Electrostatic interactions play an important role in the assembly reaction. VLPs assemble from many copies of capsid protein, with a combinatorial number of intermediates. Hence, the mechanism of the reaction is poorly understood. In this paper, we combined solution small-angle X-ray scattering (SAXS), cryo-transmission electron microscopy (TEM), and computational modeling to determine the effect of ionic strength on the assembly of Simian Vacuolating Virus 40 (SV40)-like particles. We mixed poly(styrene sulfonate) with SV40 capsid protein pentamers at different ionic strengths. We then characterized the assembly product by SAXS and cryo-TEM. To analyze the data, we performed Langevin dynamics simulations using a coarse-grained model that revealed incomplete, asymmetric VLP structures consistent with the experimental data. We found that close to physiological ionic strength, $T = 1$ VLPs coexisted with VP1 pentamers. At lower or higher ionic strengths, incomplete particles coexisted with pentamers and $T = 1$ particles. Including the simulated structures was essential to explain the SAXS data in a manner that is consistent with the cryo-TEM images.

We are delighted to dedicate this paper with lots of love to our dearest friend Philip (Fyl) Pincus, for wonderful and inspiring times together at UCSB, Israel, and all over the globe, for educating us with much generosity and excitement to clearly think about soft matter problems, and for expressing his thoughts directly and loudly with integrity and honor.

1 Introduction

About half of the known virus families have icosahedral capsids, which can, under the right conditions, spontaneously self-assemble around RNA or DNA molecules. Virus assembly is an important step in the life cycle of viruses and has become a target for antiviral research [1–13] and a model for self-assembly in nanotechnology [14–23]. Yet many details of this reaction are unknown. A simple virus may have about a hundred subunits, combinatorially more intermediates, and many more assembly pathways.

A complete description of virus assembly should include the structures of intermediates, paths between intermediates, rate constants for each step, and the stability of the species. Resolving the empty capsid assembly mechanism is already a very challenging problem [24–77], despite recent progress with experimental techniques such as resistive pulse sensing [78,79], mass spectrometry [80], charge detection mass spectrometry [81–84], and solution small-angle X-ray scattering (SAXS) [85–91]. We, however, developed a robust and transparent mechanism for isolating the most probable intermediates at equilibrium and on the assembly path of an empty Hepatitis B capsid [92]. Using MC simulations, we created a library of representative intermediates and showed that at equilibrium, a very limited number of relevant assembly reaction products are selected based on their Boltzmann weights, com-

Roi Asor and Surendra W. Singaram have contributed equally to this work.

[a] e-mail: roi.asor@chem.ox.ac.uk
[b] e-mail: swsingaram@gmail.com
[c] e-mail: yael.kalisman@mail.huji.ac.il
[d] e-mail: hagan@brandeis.edu (corresponding author)
[e] e-mail: uri.raviv@mail.huji.ac.il (corresponding author)

puted from the self-association standard free energy between subunits [93]. The analysis method assumes that intermediates can only be fragments of capsids. This approach, however, is insufficient to describe the assembly of a virus capsid around a template (e.g., a polymer chain) because the number of possible intermediates and assembly products is considerably larger (e.g., [28,30,45,63,67,68,94–120]). In addition, the structural configurations resulting from the interaction of the protein subunits with a flexible polymer cannot be captured by assuming an 'on-path' assembly mechanism based on the final capsid structure. Coarse-grained Langevin dynamics simulations offer a more advanced sampling approach, taking into account configurations beyond the capsid 'lattice.' The assembly reaction involves electrostatic interactions and hence depends on ionic strength.

In this article, we determined the effect of ionic strength on the assembly of virus-like particles (VLPs). We assembled simian vacuolating virus 40 (SV40)-like particles by mixing poly(styrene sulfonate) (PSS) with SV40 capsid virus protein 1 (VP1) pentamers. The structures of the assembly products were characterized by solution small-angle X-ray scattering (SAXS) and transmission electron microscopy at cryogenic temperatures (cryo-TEM). An earlier study [121] showed that simulations might capture experimental trends of virus capsid assembly reactions. To rigorously analyze our experimental data, we performed Langevin dynamics simulations using a coarse-grained model, accounting for the interactions between the capsid protein subunits and between the capsid protein subunits and the polymer template. The simulations provided a library of relatively stable and thus probable intermediates, obtained based on a physical model, previously shown to match observations on virus assembly around RNA and other polyanions [122,123]. We created atomic models of intermediates by docking the atomic model of the protein pentamer subunit and the PSS monomer into the simulated coarse-grained models. Using our analysis software D+ [92,124–127], we computed the solution scattering curves of each of the atomic models. We then selected the models that best explained the data and computed their mass fractions while ensuring total mass conservation.

We found that the mass fraction of pentamers, assembled into $T = 1$ SV40 VLPs, was maximal near physiological ionic strength. Decreasing or increasing the solution ionic strength changed the interactions between capsid protein subunits and between the capsid protein subunits and the polymer chain, and led to a decrease in the fraction of $T = 1$ SV40 VLPs and an increase in the fraction of free pentamers. In addition, the fraction of incomplete asymmetric VLP structures, obtained by the simulations and observed by cryo-TEM, increased. Importantly, including the simulation structures in the fitting of the SAXS data was essential to obtain conclusions that were consistent with theory and the cryo-TEM observations. The approach of combining coarse-grained simulations with analysis of SAXS profiles to identify highly asymmetric assembly structures is general and can be applied to diverse assembly systems.

2 Results and discussion

As a control, we first determined the effect of ionic strength on the assembly reaction of VP1 pentamers ($VP1_5$) in the absence of PSS at pH 7.2. We measured the solution SAXS intensity as a function of the magnitude of the scattering vector, q, from solutions of VP1 pentamers at increasing ionic strength (Fig. 1a). Above $q \sim 0.4$ the SAXS curve adequately fit the computed scattering curve from the atomic model of a hydrated VP1 pentamer (Fig. S1). At lower q values, however, the measured scattering intensity deviated from the expected value of freely diffusing VP1 pentamers. The increased scattering intensity suggests that higher-order complexes formed in the solution (Fig. 1). For noninteracting particles, the scattering intensity when $q \to 0$ is proportional to the concentration of the scattering particles and the average of their molecular weight squared [128]. Here, VP1 pentamers were measured at a fixed protein concentration of 3.75 μM while varying the ionic strength. At $q \to 0$, the ratio between the experimentally measured intensity and the soluble hydrated VP1 pentamer form-factor intensity (computed based on its atomic model taken from PDB ID 1SVA and shown in Fig. S1) provides a qualitative measure for the average mass of the particles in the sample. This intensity ratio at the lowest scattering vector (Fig. 1b) reveals that the average molecular weight of the assemblies decreased with increasing ionic strength. At the highest ionic strength (562 mM), the average molecular weight was less than two VP1 pentamers.

Cryo-TEM images at low salt concentration revealed long tubular and aggregated structures (Fig. 1c), which contributed to the enhanced and slightly oscillatory scattering intensity at $q < 0.4$ (Fig. 1a). The measured scattering intensities could be modeled as a coexistence of soluble hydrated VP1 pentamers (based on its atomic model, PDB ID 1SVA), VP1 self-assembled uniform long tubules with an inner radius of 15 nm and a wall thickness of 5 nm [129,130], and large VP1 aggregates, represented by a q^{-4} Porod law (Fig. 1a, blue curves) [131,132]. Even though the tubule model also scales as q^{-4}, it could not fit the data by itself. Similarly, q^{-4} alone was insufficient to fit the data as it did not have the weak oscillatory features observed at $q < 0.4$. The deviation from the pentamer model decreased with ionic strength (shown in Fig. S1), and as a result, the fraction of tubules and aggregates decreased with ionic strength, in agreement with the intensity at $q \to 0$ (Fig. 1b) and cryo-TEM images (Fig. 1c). The mass fraction of soluble VP1 pentamers decreased by about 20% when decreasing the ionic strength from 562 to 87 mM. This mass fraction was converted to tubules and aggregates.

We then mixed PSS with VP1 pentamers at a 1:15 molar ratio and measured the SAXS curves as a func-

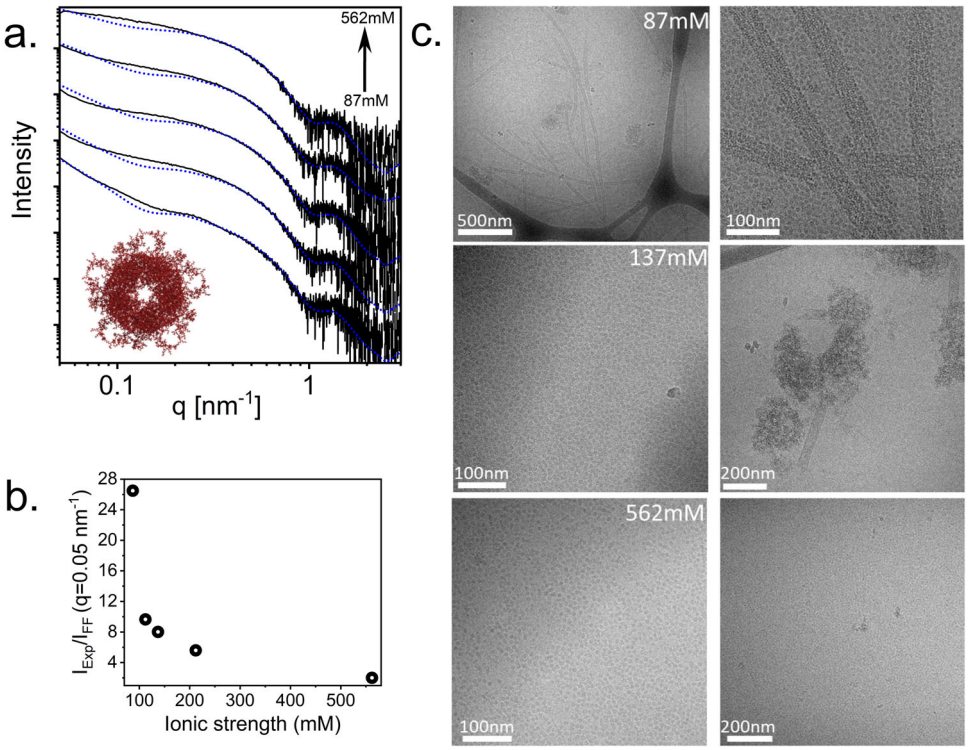

Fig. 1 Effect of ionic strength on the assembly of VP1 pentamers, in the absence of poly(styrene sulfonate) (PSS). **a** Small-angle X-ray scattering (SAXS) intensity as a function of the magnitude of the scattering vector, q, from 3.75 μM VP1 pentamers at pH 7.2 and varying ionic strengths (black curves). The curves were horizontally shifted for clarity of presentation. The computed scattering intensity curves (blue) are linear combinations of a q^{-4} power law, representing large aggregates, a model of infinitely long tubules with uniform density (inner radius of 15 nm and a wall thickness of 5 nm) [129,130], and the computed scattering intensity of a soluble hydrated VP1 pentamer, based on its atomic structure, taken from PDB ID 1SVA (see cartoon and red curves in Fig. S1) [124,125]. **b** The ratio at $q = 0.05$ nm^{-1} between the experimental SAXS signal (I_{Exp}) and the soluble hydrated VP1 pentamer form-factor intensity (I_{FF}, red curves in Fig. S1) as a function of ionic strength. **c** Cryo-TEM measurements of 6 μM VP1 pentamers at ionic strengths of 87, 137, and 562 mM (a pair of images for each ionic strength condition)

tion of ionic strength (Fig. 2a). The scattering curves are consistent with the formation of $T = 1$ SV40 virus-like particles (VLPs) [91,121]. Comparing the absolute scattering intensity curves (Fig. 2b) shows nonmonotonic changes in the measured scattering curves as the ionic strength of the solution was increased, corresponding to a nonmonotonic change in the particles' average mass. At low ionic strength (starting from 137 mM), the scattering intensity at low angles was stronger than at higher ionic strength. This result is consistent with a higher average molecular weight at lower ionic strength, as observed with VP1 pentamers in the absence of PSS (Fig. 1a). In addition to $T = 1$ VLPs (each containing 12 VP1 pentamers around a PSS chain), excess free VP1 pentamers contributed to the scattering intensity. Nevertheless, the number of possible structures that may form when PSS interacts with VP1 pentamers is immense because of the number of possible PSS chain conformations and the number of ways that each conformation can interact with the VP1 pentamers. At equilibrium, however, the number of dominant structures is likely to be much smaller, and their mole fraction is set by their excess stability with respect to the reactants (PSS and VP1 pentamers) [121].

To rationally unravel the dominant coexisting stable structures and analyze our scattering data (Fig. 2), we performed Langevin dynamics simulations using a coarse-grained model for templated assembly of VP1 pentamers around a PSS chain. The simulation model for pentamer–pentamer interactions accounts for excluded volume and short-ranged attractions that drive assembly toward $T = 1$ capsids. The pentamer–PSS and PSS–PSS interactions include excluded volume and screened electrostatics (see Sect. 4 for details). We performed the simulations under different ionic strengths and pentamer–pentamer attraction well-depth values ($\epsilon_{\mathrm{VP1-VP1}}$).

When the simulations attained steady state, we isolated the assembled VLPs (Fig. 3a) and classified them according to their size (determined by the number of VP1 pentamers attached to the PSS chain). We docked the atomic model of a VP1 pentamer (Fig. 1a) into the simulated coarse-grained pentamer model (Fig. 3b), after scaling the simulations to the correct physical dimensions (according to the atomic model of the sub-

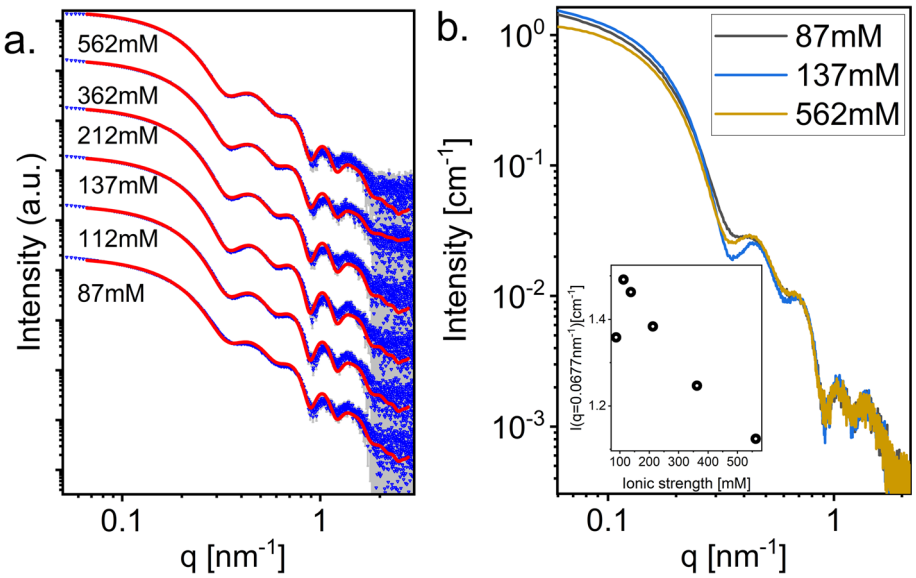

Fig. 2 Assembly of VP1 pentamers and PSS at different ionic strengths. Assembly was induced by mixing equal volumes of 0.87 μM 78 kD PSS and 13 μM VP1 pentamer aqueous solutions (i.e., the final concentrations were 0.435 and 6.5 μM, respectively) at different ionic strength conditions (see Sect. 4). **a** The SAXS curves were horizontally shifted for clarity of presentation. Each curve was fit to a linear combination of the following SAXS models, computed using D+ software [124,125]: solvated PSS-containing $T = 1$ VLP, free hydrated VP1 pentamer, and simulated models, representing possible assembly products. The fits were performed while maintaining mass conservation (Eq. 3; for a complete explanation of the pool of models, see Sect. 4). **b** Comparing the measured absolute SAXS intensity curves from representative assembly conditions. The inset shows the absolute intensity at a low scattering angle ($q = 0.0677$ nm^{-1}) as a function of ionic strength

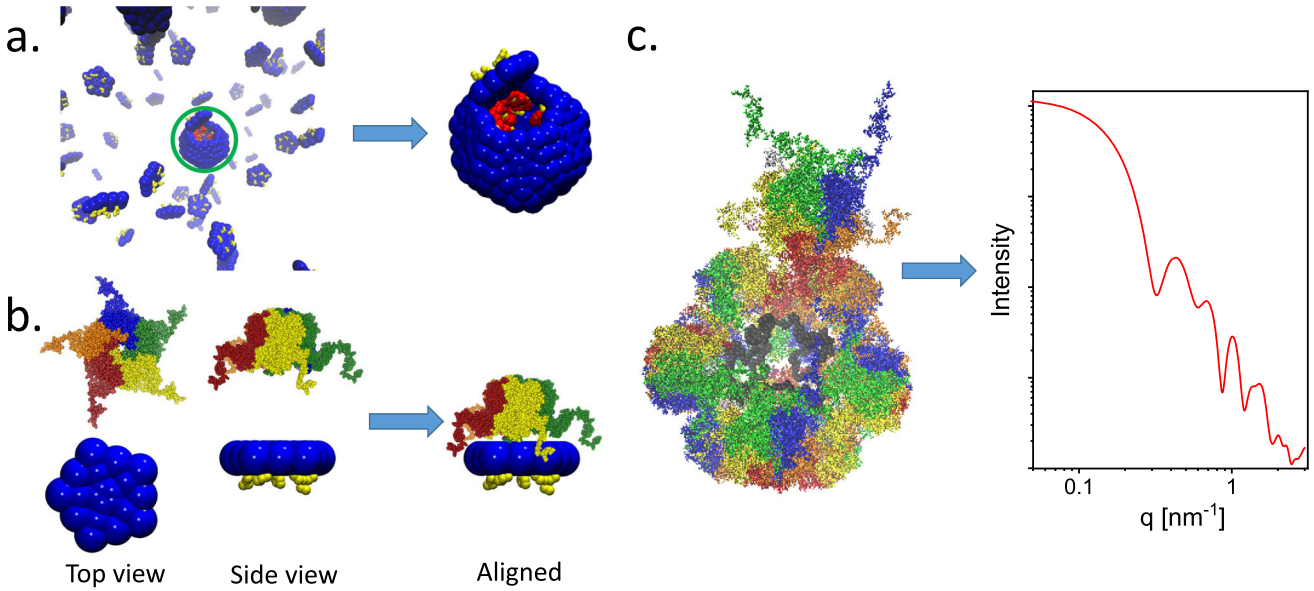

Fig. 3 Illustration of our protocol for converting the simulated coarse-grained models to atomic models for computing their solution X-ray scattering curves. **a** Isolating the assembled particle (in the green circle) from the simulation box after steady-state was attained. **b** Scaling the simulation pentamer coarse-grained model to the real-space atomic structure of VP1 pentamer (PDB ID 1SVA) and aligning the atomic structure to a reference coarse-grained subunit. **c** Computing the solution X-ray scattering curve from an atomic model of a VLP particle. The aligned reference atomic VP1 pentamer model (**b**) was docked into the isolated coarse-grained VLP assembly (**a**), accounting for symmetry by defining the rotations and translations of repeating pentamer subunits. The solution scattering curve of the VLP atomic model was computed by D+ software [124,125]. The hydration layer of the subunits and the instrument resolution function were taken into account as described in Refs. [92,126,127]

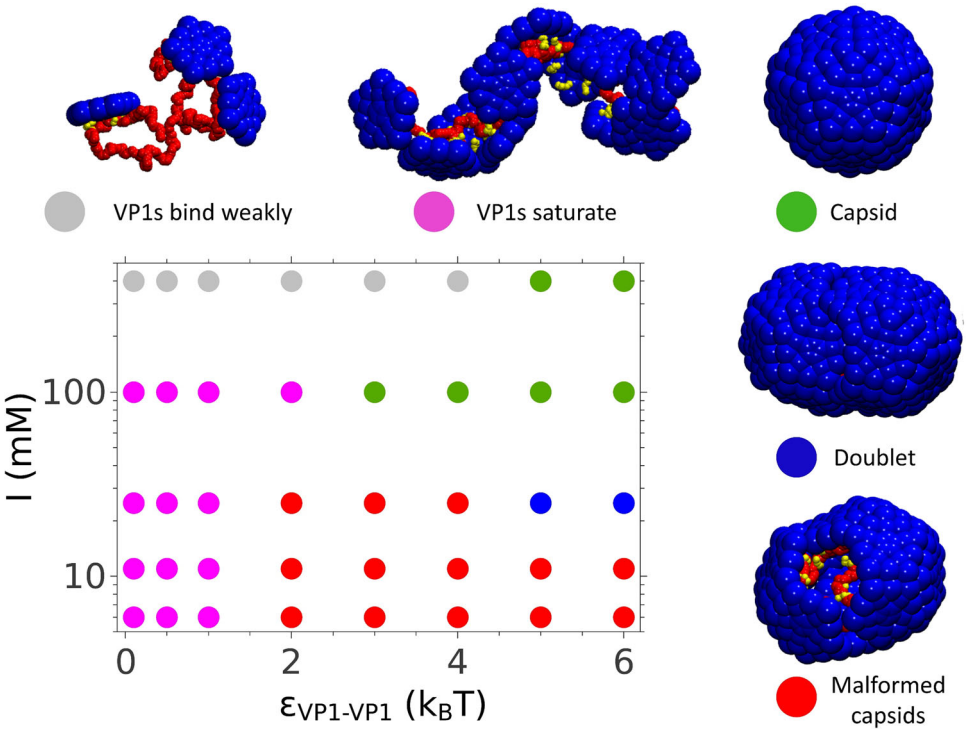

Fig. 4 The predominant assembly morphology as a function of VP1-VP1 affinity, ε, and ionic strength, I, predicted by the coarse-grained simulations. VP1 subunits were modeled as rigid pentamers, interacting with 78 kDa PSS, modeled as a 400-mer bead-spring polyelectrolyte. Morphologies are indicated by symbol color: VP1 pentamers bind weakly to the PSS (gray); VP1 pentamers saturate the PSS, but do not nucleate (pink); VP1 pentamers package the PSS in capsids with $T = 1$ symmetry (green); VP1 pentamers package the PSS in two capsids (Doublet), each with a $T = 1$ symmetry (blue); overly strong interactions drive excessive nucleation and formation of malformed capsids (red)

unit). Similarly, starting with the simulated coarse-grained PSS chain model, we docked in uniform spheres with radius and electron density parameters optimized to fit the scattering intensity from the atomic model of a styrene sulfonate monomer.

We then aligned the atomic models onto the isolated coarse-grained simulated VLP subunits (Fig. 3a), created an atomic model of the simulated VLP particle, and calculated its expected solution X-ray scattering curve, using our home-developed D+ software [124,125] (Fig. 3c).

The morphologies of the simulated VLP assemblies varied with the strength of the interaction between pentamers and ionic strength (Fig. 4). We ran many simulations under a wide range of conditions and created a diverse and representative library of relatively stable self-assembled structures. The solution X-ray scattering curve from the atomic model of each structure was computed as demonstrated in Fig. 3, and a library of representative scattering curves was created (Fig. 5). In addition, we computed a series of scattering curves from models of incomplete empty $T = 1$ VLPs, containing between 1 and 12 VP1 pentamers on the $T = 1$ lattice (Fig. S2). The typical $T = 1$ oscillations are observed when the capsid is half complete or larger (Fig. S2).

We could adequately fit the data when using the scattering curves of $T = 1$ SV40 VLPs, VP1 pentamers, and the simulated assemblies (Fig. 2a). The fraction of $T = 1$, VP1 pentamers, and simulated assemblies varied with ionic strength (Fig. 6a, b). This variation can be understood as follows. The electrostatic self-repulsion between the negatively charged outer surfaces of the VP1 pentamers scales as the Debye screening length, λ_D, whereas the attractive interaction between the negatively charged PSS and the positively charged inner surface of the VP1 pentamers scales as λ_D^4 [133]. Hence, the attractive PSS/VP1 pentamer interaction likely dominates at low ionic strengths but weakens more rapidly with increasing ionic strength than the VP1-VP1 repulsions (Fig. 1). Thus, above a threshold, intermediate salt concentration, the repulsions become stronger leading to a maximum in $T = 1$ capsid assembly at an intermediate salt concentration and a minimum in the concentration of free VP1 pentamers (Fig. 6a), in agreement with an earlier theoretical prediction [133].

In addition to capsids and free pentamers (which were in excess), the attractive interaction between PSS and the VP1 pentamers and the self-repulsion between VP1 pentamers resulted in coexistence with incomplete, more open assemblies, observed by cryo-TEM (Fig. 7). The simulated coexisting assemblies (Figs. 4, 5, 6c and d) qualitatively appear similar to the particles observed by cryo-TEM (Fig. 7), and hence were

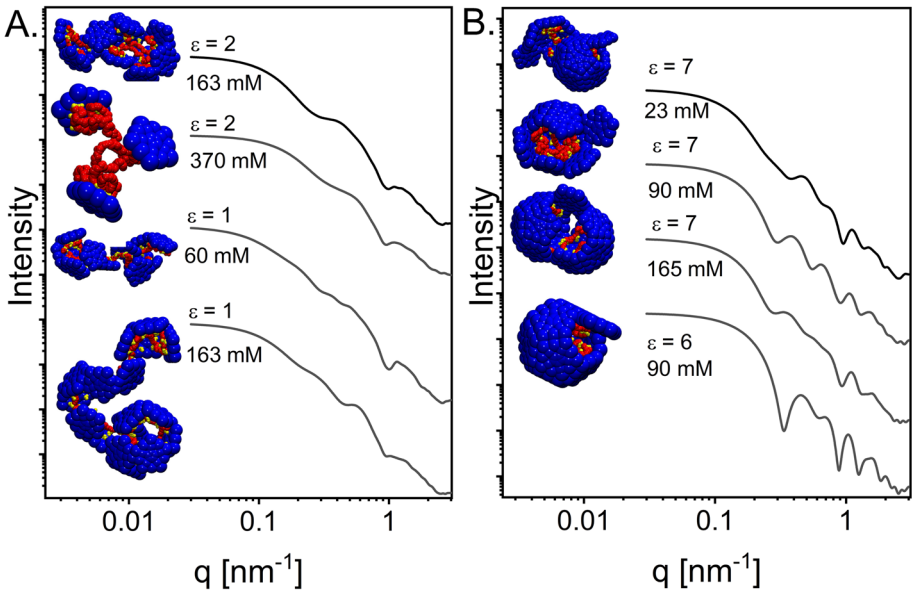

Fig. 5 Solution X-ray scattering curves from simulated VLPs under different ionic strengths (in mM) and interaction energy between pentamers, ε (in units of k_BT), as indicated. The scattering curves were computed based on atomic models of the coarse-grained VLPs as demonstrated in Fig. 3

included in the library of possible states in our analysis. The mass fraction of the simulated assemblies, which are not $T = 1$ VLPs, decreased with ionic strength to a minimum at physiological ionic strength (137 mM) and then increased with further increasing ionic strength.

Attempts to analyze the SAXS data without the library from simulations led to an adequate fit (Figs. 8, 9a) but a conclusion that was inconsistent with known physics and the coexisting additional assemblies observed by cryo-TEM (Fig. 7) and simulations (Fig. 6). In particular, fitting the data to a linear combination of the computed scattering curves from a complete $T = 1$ SV40 VLP and VP1 pentamers (a two-state model) while maintaining total mass conservation and the correct PSS:VP1 molar ratio resulted in a large (up to 20%) fraction of PSS chains that did not assemble with VP1 pentamers (and a corresponding fraction of free VP1 pentamers), even at the lowest ionic strength when the pentamer-PSS attraction was maximal (Fig. 9b, circle black symbols). Even when the mass fraction of the simulated particles was minimal (close to physiological ionic strength, Fig. 6b, circle black symbols), the two-state model led to the conclusion that about 10% of the PSS chains did not assemble with VP1 pentamers (Fig. 9b). In contrast, when including the library of simulated assemblies in the fit, most of the negatively charged PSS chains assembled with the positively charged residues of the VP1 pentamer throughout the entire range of salt concentrations (Fig. 9b, square blue symbols). This conclusion is consistent with theoretical expectations and is supported by the simulations, which always showed complexes between PSS chains and VP1 pentamers (Figs. 4, 5).

The average number of pentamers per particle was calculated by $\sum_i i\chi_i$, where χ_i is the mass fraction of particles, containing i pentamers. Both the two-state models and the models that included the simulated structures resulted in a similar nonmonotonic average mass per particle (Fig. 9c). This result is consistent with the observed nonmonotonic scattering intensity at low angles (inset to Fig. 2b).

The information content of the SAXS data alone was insufficient to distinguish between the two-state model and the models that included additional structures from the simulations. This result suggests that the total contribution to the scattering curves from the simulation assemblies (Fig. 5) could be modeled as a linear combination of pentamers and $T = 1$ capsids. When the particles are compact, their scattering curves resemble the scattering from a $T = 1$ particle, and when the structures are open their scattering curves resemble the scattering curve of VP1 pentamers. The two-state model thus appeared to be a simple way to interpret the SAXS data. However, the cryo-TEM data revealed additional structures similar to the simulated structures. Furthermore, the excess VP1 pentamers may form additional structures without PSS chains (Fig. 1). Hence, based on all the available data, the two-state model provided a less accurate interpretation of the SAXS data than the state including the simulation library. Crucially, this result highlights the importance of additional observations when analyzing complex structures with SAXS.

At a fixed ionic strength (137 mM), we varied the molar ratio between PSS and VP1. Our analysis shows that the contribution of free VP1 pentamers was minimal at a PSS:VP1 molar ratio of 1:12 (the expected $T = 1$ stoichiometry) and increased with the molar fraction of added VP1 (Fig. 10). The fraction of VP1 pentamers forming incomplete complexes was rather small ($\approx 10\%$) at the stoichiometric PSS:VP1 molar ratio and with about 25% excess of VP1 pentamers. Most PSS chains formed complete $T = 1$ particles with a greater excess of VP1 (1:18).

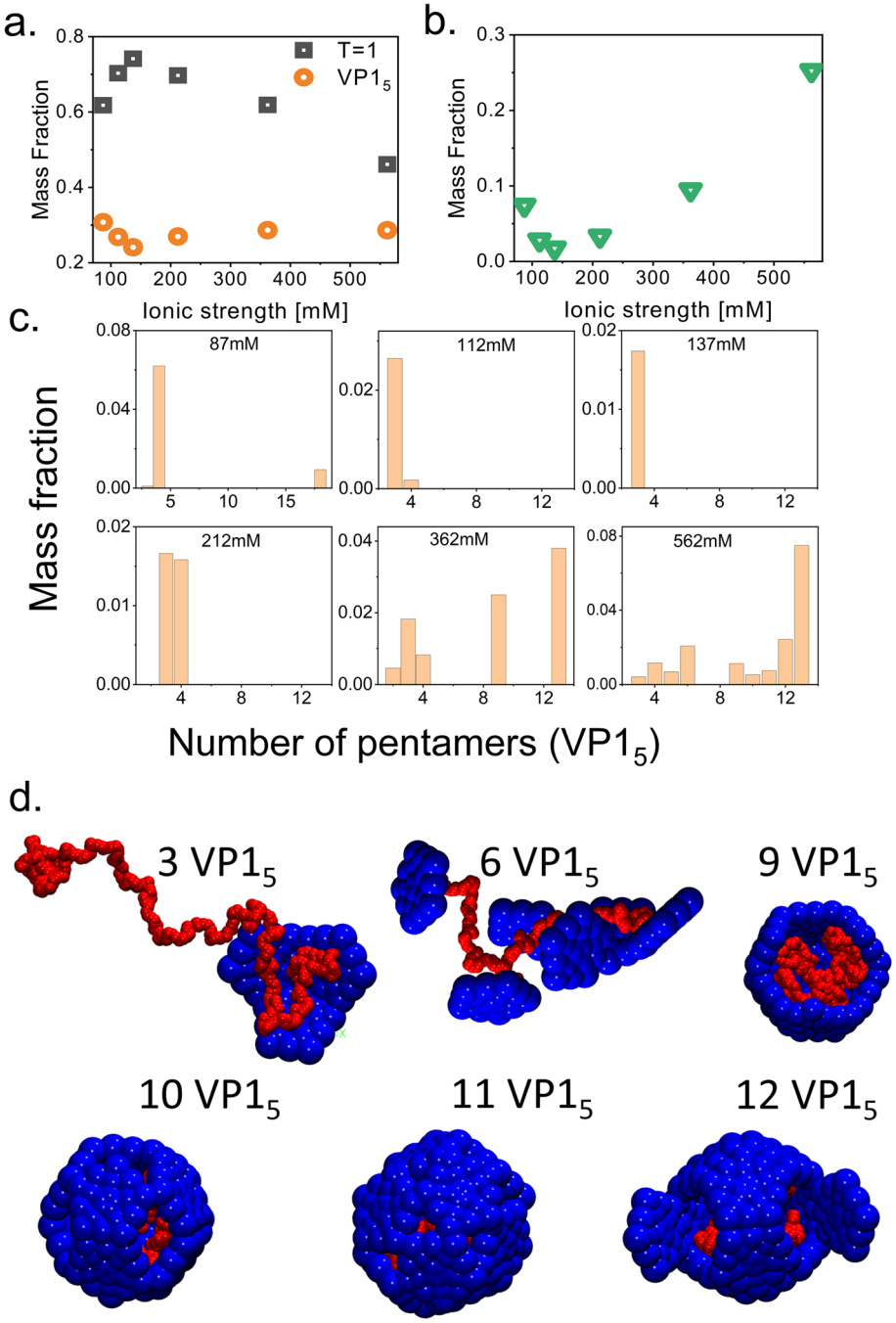

Fig. 6 Dominant assembly states of PSS-containing VLPs at pH 7.2 and the indicated ionic strengths. **a** Mass fractions of the two dominant populations as a function of ionic strength, based on the SAXS analysis. Black square symbols correspond to the contribution of $T = 1$ PSS-containing VLPs. Orange circle symbols correspond to the contribution of VP1 pentamers. **b** The total mass fraction of incomplete simulated PSS-VP1 assemblies as a function of ionic strength. **c** The distributions of the total mass presented in panel b as a function of the size (number of VP1 pentamers) of the simulated assembled states. The ionic strength is indicated in each histogram. **d** Examples of coarse-grained structures, selected by the SAXS curve fitting procedure. The number of VP1 pentamers incorporated in each assembled structure is indicated

3 Conclusions

In this paper, we combined SAXS, cryo-TEM, and Langevin dynamics simulations to unravel the effect of ionic strength on the assembly of SV40 VP1 pentamers around a charged polymer template. We found that free VP1 pentamers coexisted with $T = 1$ VLPs as well as incomplete asymmetric structures. Close to physiological ionic strength, the mass fraction of incomplete structures was minimal, consistent with other virus systems (e.g., [27,29,46,50,51,134–137]). The mass fraction of incomplete structures increased when the ionic strength deviated from the physiological ionic strength toward lower or higher ionic strengths (and changed the interaction between subunits). The morphologies of the incomplete particles, predicted by the simulations, were qualitatively consistent with cryo-TEM images and essential for a rigorous analysis of the SAXS data. Our results demonstrate that such additional observations are essential to unambiguously interpret SAXS data for complex systems. Our approach is broadly applicable to self-assembly reactions and provides a means to elucidate the ensemble of structures for complex systems involving a large number of subunits and an immense number of possible products. In the future, our approach can be used to study the effect of ionic composition or added crowding agents on the assembly reaction.

Finally, while we focused on the equilibrium product distribution in this article, our approach may also be applied to analyze time-resolved SAXS (with msec temporal resolution) [91] to identify the structures of assembly intermediates and their dynamics as was recently demonstrated [92]. Simulations can create a comprehensive library of distinct intermediates and compute their relative stability. The library can be used to compute a prior distribution, fitted to either the onset or the end of an assembly reaction. The prior distributions of other time points can be the fitted distributions of earlier and successive time points, making the optimization more robust, which in combination with maximum entropy optimization may be used to fit an entire time-resolved SAXS data sequence [92].

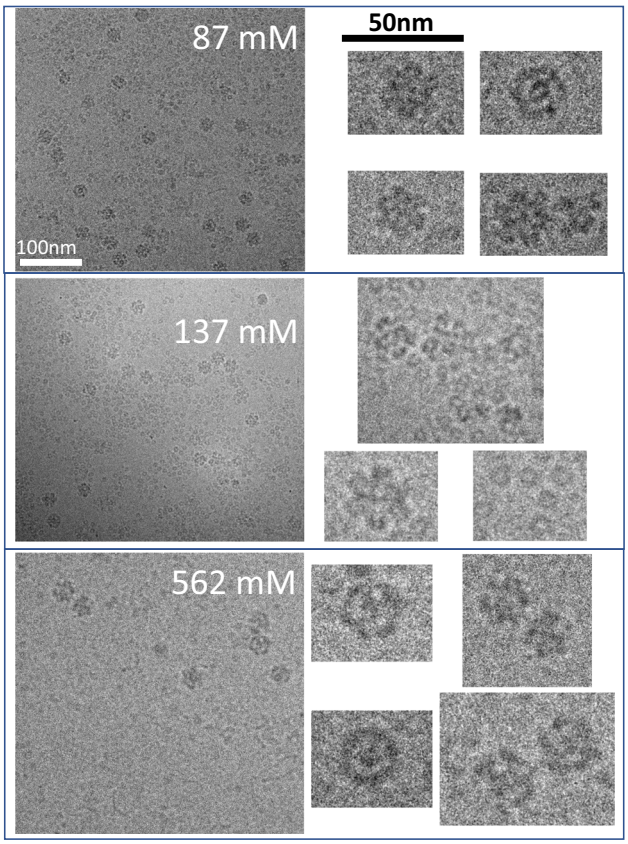

Fig. 7 Cryo-TEM images of the dominant PSS and VP1 pentamers assembly reaction products at pH 7.2 at three representative ionic strengths (87, 137, and 562 mM). The final concentrations of VP1 pentamers and PSS were 6 μM and 0.4 μM, respectively. For each ionic strength condition (indicated in the figure), a selected set of particles is shown on an expanded scale on the right side

4 Materials and methods

4.1 Sample preparation

4.1.1 VP1 production and purification

VP1 virus-like particles (VLPs) were produced as previously described in Spodoptera frugiperda (sf9) cells, using baculovirus expression vector [138]. VP1-VLPs were then purified from nuclear extract using CsCl density gradient centrifugation. Nuclear extracts were 2-fold diluted with 0.5M NaCl solution and added to a concentrated CsCl solution, adjusted to a final density of 1.3 g/mL. The nuclear extract suspension was centrifuged in a Beckman 13.2 mL, open-top Thinwall polypropylene tube (cat. number 331372) in SW41 Ti Swinging Bucket rotor at 38,000 RPM for 40 h. Following centrifugation, VP1-VLPs could be detected by scattered light, as a thick white band in the middle of the tube. The band was pulled and rebanded using a second centrifugation. The fractions were analyzed to assess VP1 content using SDS-polyacrylamide gel electrophoresis (Novex WedgeWell 4–12% Tris-Glycine) with Coomassie-Blue staining (Instant blue stain, Expedeon). VP1-VLPs were dialyzed against 0.5 M NaCl at 4 °C using GeBa dialysis tubes with a cutoff of 8 kDa (Gene Bio Application Ltd. cat. no. D070-6). Two dialysis cycles were applied, 1.5 h each, against bulk solutions, whose volumes were 1000× the VP1-VLPs suspension volume. VP1-VLPs were stored up to a month at 4 °C.

4.1.2 Preparing VP1 pentamers solution for assembly reactions

Polymer-containing VLP (pcVLP) assembly followed the disassembly-reassembly procedure described earlier [91]. Briefly, the purified VP1-VLPs were first disas-

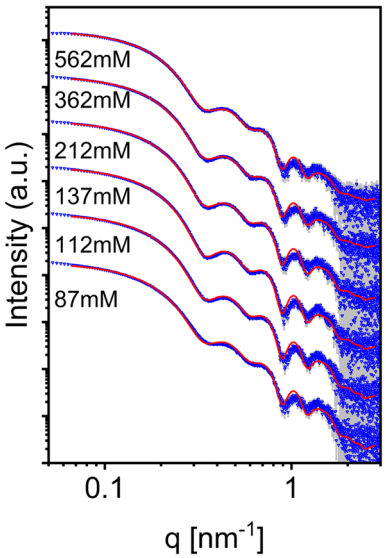

Fig. 8 Fitting the solution X-ray scattering data from Fig. 2 using a linear combination of two states: the computed scattering curves from atomic models of hydrated VP1 pentamers (Fig. S1) and the complete $T = 1$ SV40 VLPs. The fits were performed while maintaining mass conservation (Eq. 3)

sembled, using two dialysis cycles against disassembly buffers. VP1-VLPs were first dialyzed against disassembly buffer A, containing: 20 mM Tris at pH 8.9, 2 mM DTT, 5 mM EDTA and 50 mM NaCl, followed by a second dialysis against disassembly buffer B, which was similar to buffer A but contained only unit 2 mM EDTA (instead of 5 mM). Both dialysis cycles were performed at 4 °C for 1.5–2 h each, where the ratio between the bulk solution volume and the VP1-VLPs suspension volume was greater than 1000. Following disassembly, the solution containing VP1 pentamers was centrifuged at 20,000g for 40 min at 4 °C to precipitate larger oligomers. The concentration of VP1 pentamers was measured using UV–Vis absorption spectroscopy with an extinction coefficient of $32,890\,\mathrm{M}^{-1}\mathrm{cm}^{-1}$ for a VP1 monomer.

4.1.3 VP1-PSS measurements

The reactions were initiated by mixing equal volumes of 13 μM (data in Figs. 2 and 7) or 10.6 μM (data in Fig. 8) VP1 pentamers in disassembly buffer B (20 mM 2-Amino-2-hydroxymethyl-propane-1,3-diol (Tris), pH 8.9, 2 mM DTT, 2 mM EDTA and 50 mM NaCl) with 0.87 μM (Figs. 2, 7) or varying concentrations (Fig. 8) of 78 kDa polystyrene sulfonate (PSS) solutions, containing 100 mM 3-morpholinopropane-1-sulfonic acid (MOPS) buffer (pH 7.2) and different concentrations of NaCl. SAXS measurements were taken following incubation for at least 5 h at ambient room temperature.

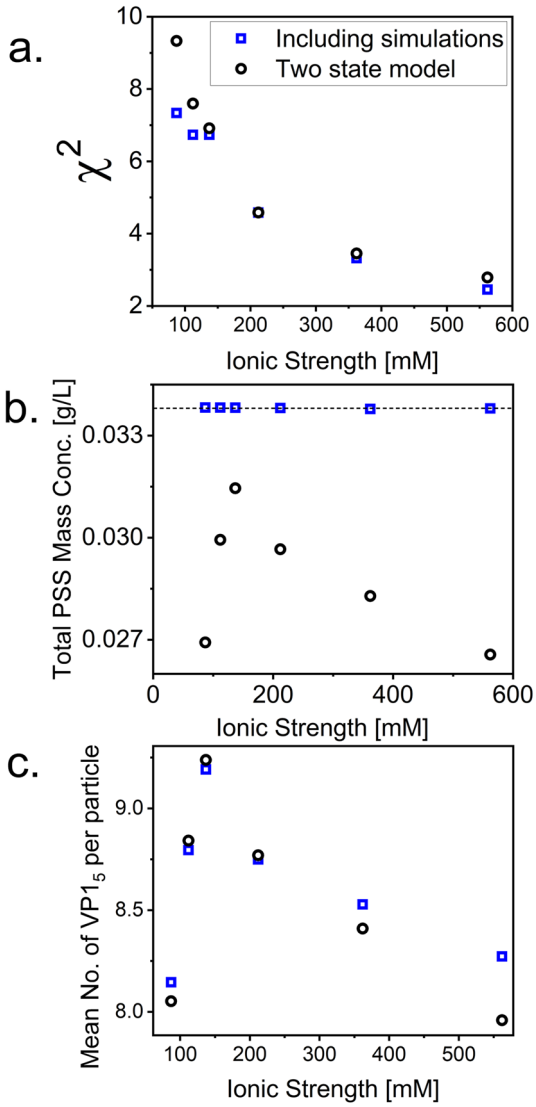

Fig. 9 Comparing the SAXS data analysis with (open square blue symbols) and without the simulated assemblies (open circle black symbols). **a** The Chi-square values of the fit from Fig. 8 using the two-state model (circle symbols) and the fit from Fig. 2a with the simulated assemblies (square symbols) as a function of ionic strength. **b** The total PSS mass concentration of assembled PSS chains as a function of ionic strength when fitting the data with (square symbols) and without (circle symbols) the simulated assemblies. **c** The average number of VP1 pentamers per particle as a function of ionic strength when fitting the data with (square symbols) and without (circle symbols) the simulated assemblies

4.1.4 VP1 pentamer assembly in the absence of PSS

PSS-free assembly reactions of VP1 at each solution condition were initiated by mixing equal volumes of 7.5 μM VP1 pentamers in disassembly buffer B with buffered solutions, containing 100 mM MOPS buffer at pH 7.2 and different NaCl concentrations. All samples

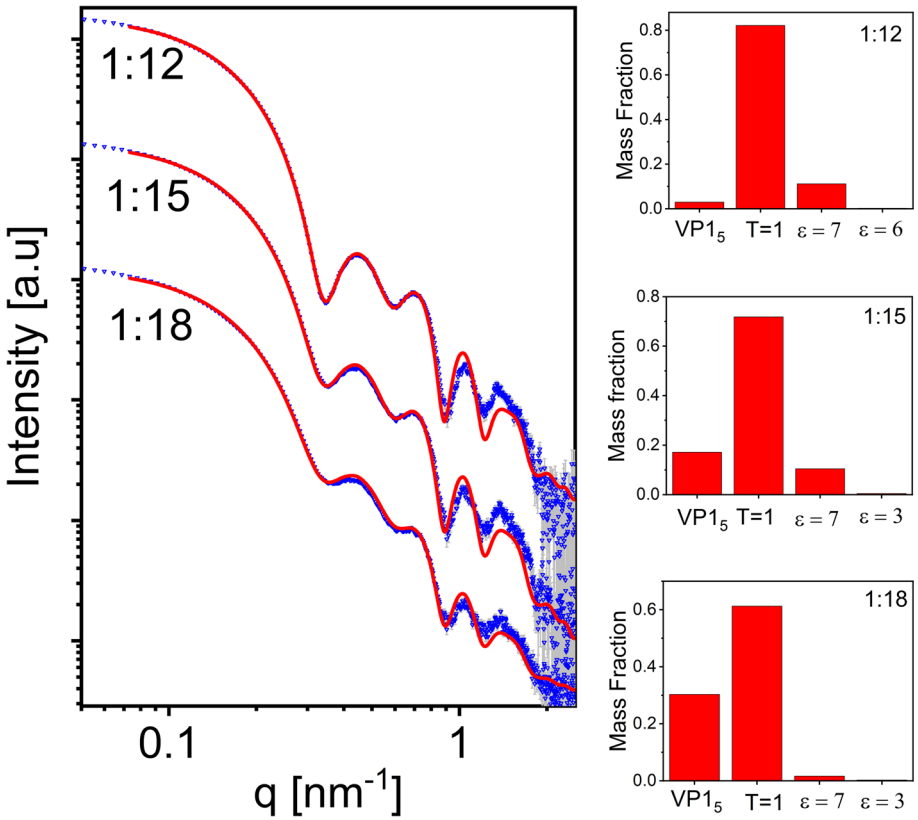

Fig. 10 SAXS analysis of assembly reactions at different PSS to VP1 molar ratios. Assembly was performed at a fixed ionic strength (137 mM) and induced by mixing equal volumes of 10.6 μM VP1 pentamer solution with varying concentrations of 78 kD PSS solution leading to the indicated molar ratios. Each SAXS curve was fit to a linear combination of the following modeled scattering curves: free hydrated VP1 pentamer, hydrated PSS-containing $T = 1$ VLP model, and simulated models of VP1 - PSS complexes, representing likely assembly products with the indicated interaction strength, ε, values. The modeled scattering curves were calculated using D+ software [124,125]. The histograms on the right show the mass fraction of pentamers in each model with a resultant mass fraction above 0.01. The scattering curves were horizontally shifted for clarity of presentation

were measured following several hours of incubation at ambient room temperature.

4.2 SAXS measurements

Solution small-angle X-ray scattering (SAXS) measurements were taken at the P12 EMBL Beamline (headed by D. Svergun) in PETRA III (DESY, Hamburg) [139]. Measurements were taken using an automated sample changer setup as described [92,93,140]. The wavelength of the incident X-ray beam was 1.24Å, and the scattering intensity was recorded on a single-photon PILATUS 2 M pixel area detector (DECTRIS). The sample to detector distance was 3.1m. Thirty–forty microliters of each sample was injected in each measurement, and 25 frames were recorded with an exposure time of 45 ms per frame. Initial reduction of the scattering signals to one-dimensional curves of scattering intensity as a function of the magnitude of the scattering vector, q, was performed using the P12 pipeline [141].

Background measurements before and after each sample were taken on the solvent of each sample, under identical measurement conditions. Both background and sample scattering curves were averaged over all the frames, and the averaged background signal was subtracted from the averaged sample and gave the final background subtracted scattering intensity curve of the assembly reactions, as explained in our earlier papers [92,124–127]. All the assembly reactions were measured at 25 °C.

SAXS measurements were also taken at the ID02 beamline (headed by T. Narayanan) in the European synchrotron radiation facility (ESRF, Grenoble). Measurements were taken using the flow-cell setup, which included a temperature-controlled, 2 mm thick, quartz capillary [142,143]. The wavelength of the incident beam was 0.995Å, and the scattered intensity was recorded on a Rayonix MX170-HS detector [143,144]. Data reduction was performed using SAXSutilities software.

4.3 Cryo-TEM measurements

Assembly reactions for cryo-TEM measurements were prepared using a protocol identical to the protocol used for SAXS measurements. The final concentrations of VP1 and PSS were 6 μM and 0.4 μM, respectively. All assembly reactions were incubated at ambient room temperature for ∼24 h. Sample preparation and image acquisition were performed as described in our earlier publication [86].

4.4 Coarse-grained computational model

To develop a library of intermediate structures, we performed Langevin dynamics simulations with a coarse-grained model for the assembly of $T = 1$ SV40 VLPs around a polyelectrolyte. The model is adapted from models previously used to simulate the assembly of empty capsids [64,145,146], which were extended to model assembly around RNA and other substrates in Refs. [122,123,147–150].

The $T = 1$ SV40 VLP capsid is modeled as a dodecahedron composed of 12 pentagonal subunits. The subunits are attracted to each other by an attractive Morse potential between Attractor ('A') pseudoatoms at each subunit vertex. The Top ('T') pseudoatoms interact with other 'T' pseudoatoms through a potential consisting of the repulsive term of the Lennard–Jones (LJ) potential, the radius of which is chosen to favor a subunit-subunit angle consistent with a dodecahedron (116 degrees). The Bottom ('B') pseudoatom has a repulsive LJ interaction with 'T' pseudoatoms, to prevent 'upside-down' assembly. The 'T,' 'B,' and 'A' pseudoatoms form a rigid body [64,145,146]. To represent the capsid shell excluded volume more accurately than the original model, we add a layer of 'Excluder' pseudoatoms, having a repulsive LJ interaction with the polyelectrolyte and the ARMs (discussed next). The attraction strength is controlled by the model parameter ε. In Ref. [123], the relationship between the potential well-depth ε and the dimerization standard Helmholtz free energy was estimated to be $g_{ss}/k_BT = 1.5 - 5.0\varepsilon/k_BT$.

We represent the PSS with a linear bead-spring polyelectrolyte, with a charge of -e per bead. To represent the SV40 capsid protein RNA binding domains (arginine rich motifs, ARMs), we affix flexible polymers to the inner surface of each model capsid subunit. There are 5 ARMs per capsid subunit (since it is a homopentamer). While in previous work [123] we simulated ARMs with both charged and neutral segments, in this work each ARM contains only 5 positively charged beads for simplicity. The first segment of each ARM is part of the subunit rigid body, whereas the remaining ARM segments are not rigid but connected to the rigid body through the bonded interactions within each ARM. Each ARM is modeled as a bead-spring polymer, with one bead per amino acid. The 'Excluders' and first ARM segment are part of the subunit rigid body. ARM beads interact through repulsive LJ interactions and, if charged, electrostatic interactions modeled by a Debye–Hückel (DH) potential.

Electrostatics are modeled using DH interactions, where the Debye screening length (λ_D) is determined by the ionic strength I_S as $\lambda_D \approx 0.3/I_S^{1/2}$ with λ_D in nm and I_S in molar units. We consider monovalent salt, for which I_S is given by the salt concentration C_{salt}. Perlmutter et al. [122] showed that DH interactions compare well to simulations with explicit counterions for the parameter values under consideration; however, we note that the DH approximation is less accurate at lower salt concentrations.

Simulations and units Simulations were performed with the Langevin dynamics algorithm of HOOMD, which uses the Langevin equation to evolve positions and rigid body orientations in time [151–153]. Simulations were performed using a set of fundamental units. The fundamental energy unit is selected to be $E_0 \equiv k_BT$. The unit of length D_0 is set to the circumradius of a pentagonal subunit, which is taken to be $D_0 \equiv 5$ nm so that the dodecahedron inner radius is $1.46D_0 = 7.3$ nm, which is on the order of the size of a $T = 1$ SV40 VLP.

The library of simulation structures is composed of representative samples from thermally equilibrated ensembles. Assembly simulations were performed at least 10 times for each set of parameters, with each simulation concluded at either completion, persistent malformation, or 1×10^8 time steps. For all dynamics simulations, there were 30 subunits in a box with dimensions $75 \times 75 \times 75$ nm^3, resulting in a concentration of 120 μM $VP1_5$. The simulations employed periodic boundary conditions.

4.5 Analyzing the SAXS signals

4.5.1 Calculation of SAXS intensities from coarse-grained Langevin dynamics simulations

To compute the expected solution X-ray scattering intensity curves from the polymer-VP1 pentamer complex in D+ software [124,125,154–156], we used the atomic model of a VP1 pentamer (taken from PDB ID 1SVA) and a small sphere representing the PSS monomer. We docked the VP1 pentamer atomic model into its assembly symmetry, describing the manner by which copies of a subunit are shifted and rotated.

Generating assembly symmetry files from the simulation frames: An equilibrated MD simulation trajectory included 4 saved frames. Each frame included the size and shape of the box (3 edges and 3 angles between them) and a list of 3D bead coordinates (a polymer contained 400 beads, each VP1 pentamer contained 22 beads, and each simulation included a polymer chain and 30 VP1 pentamers). Each pentamer contained a list of 22 consecutive bead coordinates (using periodic boundary conditions), 20 of which defined the rigid core, whereas the top and bottom beads defined its inner and outer faces, respectively. The simulation frames did not include the coarse-grained representa-

tions of the N-terminal ARMs. The polymer chain interacted with the pentamers and formed complexes that coexisted with free pentamers.

A Python program identified the pentamers that formed a complex with the polymer and computed the assembly symmetries of the VP1 pentamers and the polymer subunit, based on the MD simulation frames. An assembly symmetry contains the manner by which copies of a subunit are shifted and rotated and was required for computing the X-ray scattering curve of a complex in D+ software (Fig. 3).

Each equilibrated simulation frame was corrected for periodic boundary conditions by surrounding the simulation box with 26 copies of its translated pentamer beads.

We identified the coordinates of fragmented subunits near the periodic boundaries if the distance between beads and the geometric center of the pentamer was larger than the pentamer enclosing radius. To correct the coordinate list of these subunits, we applied a k-means clustering algorithm with an initial guess of 8 clusters [157]. If the separations between the resultant centroids were smaller than the size of a pentamer, the clusters were merged, and the number of clusters was modified. A second k-means procedure was applied with the modified number of clusters as an input parameter, and the resultant clusters defined the subunit fragments. The fragments were then combined by a series of translations.

To isolate the VP1-polymer complex (Fig. 3a), as a first step, VP1 pentamer subunits within an interaction distance of 1.5 in the simulation units (where 1 in the simulation units equals 4.6 nm) between the geometric center of the pentamer and the polymer beads were considered to be part of the complex. The remaining pentamers were initially considered free. A free pentamer, interacting with any of the pentamers in a complex, was added to the complex. This was repeated until no free pentamer had to be added. The interaction cutoff distance between two pentamers was set to 0.6 in the simulation units between the most peripheral beads of these pentamers. (The 5 peripheral beads of each pentamer were located at the largest distance from its geometric center.)

A reference subunit was aligned such that its geometrical center was at the origin, and its director (the vector connecting the bottom and top bead centers) was aligned with the positive z axis (Fig. 3b). To extract the position and orientation of each pentamer in the complex, the rotation Euler angles and translation vectors were calculated with respect to the aligned reference subunit. The output of the calculation included a list of the geometric centers and Euler angles of each pentamer in the complex and the geometric centers of the polymer subunits. The exported positions were multiplied by an optimized scaling factor of 4.6, representing the ratio between the real-space and simulated VP1 pentamer dimensions (obtained by comparison with scattering data), and translated such that the center of mass of the pentamers was located at the origin.

Docking of the VP1 pentamer atomic structure: To compute the solution X-ray scattering curves from VP1-polymer complex in D+ software [124,125], we first aligned an atomic model of a VP1 pentamer, taken from PDB ID 1SVA and a published cryo-TEM data [90], with the coarse-grained reference subunit. The center-of-mass of the pentamer atomic model was located at (0,0, 2.6 nm), and the alignment of the pentamer C-arms was compared with the attractor beads in the coarse-grained reference subunit. The alignment was validated by comparing the computed scattering curve of a $T = 1$ particle from the Langevin dynamics simulations with the computed scattering curve based on a published cryo-TEM $T = 1$ SV40 virus-like particle structure [90]. The scattering amplitude of the hydrated VP1 pentamer was computed in D+, using a solvent probe radius of 0.14 nm, a hydration layer thickness of 0.2 nm, and a mean electron density of 364 e/nm^3.

Docking of the styrene sulfonate monomer: The orientation-averaged scattering intensity from an atomic model of a styrene sulfonate monomer (CID 75905) was computed and fitted to a sphere model with a radius of 0.23 nm, and a mean electron density of 1208e/nm^3. The contribution of the PSS polymer was computed by docking the best-fitted sphere model into the assembly symmetry of the 400 polymer subunits, obtained from the Langevin dynamics simulations.

4.6 Fitting the SAXS data

The scattering data were fitted to a linear combination of the following computed scattering curves:

1. *Computed free VP1 pentamer:* The solution SAXS intensity from the atomic model of a free VP1 pentamer (taken from PDB ID 1SVA) was computed with a hydration shell, computed by D+ program [124,125] with a solvent probe radius of 0.14 nm, a hydration layer thickness of 0.2 nm, and a mean electron density of 364 e/nm^3.
2. $T = 1$ *SV40 virus-like particle:* The atomic model of the $T = 1$ SV40 virus-like particle was created by docking the VP1 atomic pentamer model and the spherical polymer subunits to a complete $T = 1$ particle taken from a simulation frame (as explained above). The structure was further modified by adding an inner uniform sphere, represented by a hyperbolic tangent model with a radius of 5.5 e/nm^3, maximum electron density of 378 e/nm^3, and a slope of 0.8, as explained in Ref. Thermal fluctuations were taken into account by allowing the center of mass of the VP1 pentamers to fluctuate about their position. The fluctuation amplitude was randomly drawn from a uniform distribution between −0.5 and 0.5 nm. The scattering model represents an average of 15 generated $T = 1$ particles.
3. *A library of VP1-polymer complexes:* The library was generated by coarse-grained MD simulations, using a range of pentamer–pentamer interaction

parameters ($3 \leq \varepsilon \leq 7$) and Debye lengths ($0.5\,\text{nm} \leq \lambda_D \leq 1\,\text{nm}$).

4.6.1 Constrained data fitting

The fitting algorithm included a least-squares fitting of the model to the data, where the contribution of each component, representing its mass fraction, had to be nonnegative and obey the constraint of total mass conservation. The total modeled scattering intensity can be written as $I_{\text{Total}}(q) = sM_{\text{Total}} \sum_i \chi_i I(q)_i$, where χ_i is the mass fraction of material found in state i, $I(q)_i$ is its normalized scattering curve per 1 g/L, $M_{\text{Total}} = m_{\text{VP1}} + m_{\text{PSS}}$, is the total mass concentration in the sample and s is a fitted scaling factor to convert the modeled scattering curves to the signal absolute scale. Since VP1 pentamers are the major contributors to the total scattering intensity, we can assume that $M_{\text{Total}} \approx m_{\text{VP1}}$. This assumption was justified by the higher concentrations of the VP1 pentamers compared with the PSS polymer (15:1) and the corresponding higher molecular mass (210 kDa compared with 78 kDa). The two conservation laws can be therefore written as,

$$\sum_i \chi_i = 1 \tag{1}$$

for the mass conservation of the VP1 pentamers and as

$$M_{\text{Total}} M^{\text{w}}_{\text{PSS}} \sum_{i \neq \text{VP1}_5} \frac{\chi_i}{M^{\text{w}}_i} \leq m_{\text{PSS}} \tag{2}$$

for the PSS polymer, where M^{w}_i and $M^{\text{w}}_{\text{PSS}}$ are the molecular weights of the VP1_5-PSS complex and the molecular weight of the polymer, respectively.

To take into account the conservation laws and our lack of sensitivity to accurately measure the residual PSS polymer in solution, the minimized cost function, g, for the fitting was

$$g = \frac{1}{n_q - 1} \sum_{q_i = q_{\min}}^{q_{\max}} \left(\frac{I_{\text{Total}}(q_i) - I_{\text{signal}}(q_i)}{\sigma_{q_i}} \right)^2 + \lambda \cdot \Delta \tag{3}$$

where Δ is

$$\Delta = \begin{cases} \left(\frac{m^{\text{model}}_{\text{PSS}}}{m_{\text{PSS}}} - 1 \right)^2, & \text{if } m^{\text{model}}_{\text{PSS}} > m_{\text{PSS}} \\ 0, & \text{otherwise} \end{cases} \tag{4}$$

where,

$$m^{\text{model}}_{\text{PSS}} = M_{\text{Total}} M^{\text{w}}_{\text{PSS}} \sum_{i \neq \text{VP1}_5} \frac{\chi_i}{M^{\text{w}}_i} \tag{5}$$

and λ is a regularization parameter set to 10^3.

Supplementary information. The Supporting Information includes three additional supporting figures.

Supplementary information The online version contains supplementary material available at https://doi.org/10.1140/epje/s10189-023-00363-x.

Acknowledgements We thank Orly Ben-nun-Shaul and Ariella Oppenheim for assistance with VP1 purification and Daniel Harries for helpful discussions. We acknowledge the European Synchrotron Radiation Facility (ESRF) beamline ID02 (T. Narayanan and his team), the Desy synchrotron at Hamburg, beamline P12 (D. Svergun and his team), and Soleil synchrotron, Swing beamline (J. Perez and his team), for provision of synchrotron radiation facilities and for assistance in using the beamlines.

Funding This work was supported by Award Number R01GM108021 from the National Institute Of General Medical Sciences, the Brandeis Center for Bioinspired Soft Materials, an NSF MRSEC (DMR-2011846), and by the Israel Science Foundation (1331/20). Computational resources were provided by the NSF XSEDE and ACCESS allocation TG-MCB090163 and the Brandeis HPCC, which is partially supported by the NSF through DMR-MRSEC 2011846 and OAC-1920147. R.A. acknowledges support from the Kaye-Einstein Fellowship Foundation.

Author contribution statement

All authors were involved in designing the project, discussed the results, and commented on the manuscript. RA and UR performed the SAXS measurements, RA and YLK performed cryo-TEM measurements SWS and MFH performed Langevin dynamics simulations. RA wrote the code to integrate Langevin dynamics simulations with SAXS analysis. RA and UR analyzed the SAXS data. RA, MFH, and UR drafted the manuscript. MFH and UR supervised the work.

Availability of data and materials Data will become available upon request.

Declarations

Conflict of interest/Conflict of interest: The authors declare no conflict of interest/Conflict of interest.

Ethics approval NA

Code availability: The code of D+ is available for academic usage at https://scholars.huji.ac.il/uriraviv/book/d-0 Simulations and other codes will become available upon request.

journals: https://www.biomedcentral.com/getpublished/editorial-policies.

References

1. M. Bester Stephanie, G. Wei, H. Zhao, D. Adu-Ampratwum, N. Iqbal, V. Courouble Valentine, C. Francis Ashwanth, S. Annamalai Arun, K. Singh Parmit, N. Shkriabai, P. Van Blerkom, J. Morrison, M. Poeschla Eric, N. Engelman Alan, B. Melikyan Gregory, R. Griffin Patrick, R. Fuchs James, J. Asturias Francisco, M. Kvaratskhelia, Structural and mechanistic bases for a potent hiv-1 capsid inhibitor. Science **370**(6514), 360–364 (2020). https://doi.org/10.1126/science.abb4808
2. W.S. Blair, C. Pickford, S.L. Irving, D.G. Brown, M. Anderson, R. Bazin, J. Cao, G. Ciaramella, J. Isaacson, L. Jackson, R. Hunt, A. Kjerrstrom, J.A. Nieman, A.K. Patick, M. Perros, A.D. Scott, K. Whitby, H. Wu, S.L. Butler, Hiv capsid is a tractable target for small molecule therapeutic intervention. PLoS Pathog. **6**(12), 1001220 (2010). https://doi.org/10.1371/journal.ppat.1001220
3. S.K. Carnes, J.H. Sheehan, C. Aiken, Inhibitors of the hiv-1 capsid, a target of opportunity. Current Opinion in HIV and AIDS **13**(4) (2018)
4. K. Deres, C.H. Schroder, A. Paessens, S. Goldmann, H.J. Hacker, O. Weber, T. Kramer, U. Niewohner, U. Pleiss, J. Stoltefuss, E. Graef, D. Koletzki, R.N. Masantschek, A. Reimann, R. Jaeger, R. Gross, B. Beckermann, K.H. Schlemmer, D. Haebich, H. Rubsamen-Waigmann, Inhibition of hepatitis b virus replication by drug-induced depletion of nucleocapsids. Science **299**(5608), 893–6 (2003)
5. H.J. Hacker, K. Deres, M. Mildenberger, C.H. Schroder, Antivirals interacting with hepatitis b virus core protein and core mutations may misdirect capsid assembly in a similar fashion. Biochem. Pharmacol. **66**(12), 2273–9 (2003)
6. C.R. Hurt, V.R. Lingappa, W.J. Hansen, Chapter 17 - the emergence of small-molecule inhibitors of capsid assembly as potential antiviral therapeutics. Annual Reports in Medicinal Chemistry, vol. 46, pp. 283–297. Academic Press (2011). https://doi.org/10.1016/B978-0-12-386009-5.00010-2
7. S.P. Katen, S.R. Chirapu, M.G. Finn, A. Zlotnick, Trapping of hepatitis B virus capsid assembly intermediates by Phenylpropenamide assembly accelerators. ACS Chem. Biol. **5**(12), 1125–1136 (2010)
8. R.W. King, S.K. Ladner, T.J. Miller, K. Zaifert, R.B. Perni, S.C. Conway, M.J. Otto, Inhibition of human hepatitis b virus replication by at-61, a phenylpropenamide derivative, alone and in combination with (-)beta-l-2',3'-dideoxy-3'-thiacytidine. Antimicrob. Agents Chemother. **42**(12), 3179–86 (1998)
9. R.B. Perni, S.C. Conway, S.K. Ladner, K. Zaifert, M.J. Otto, R.W. King, Phenylpropenamide derivatives as inhibitors of hepatitis b virus replication. Bioorg. Med. Chem. Lett. **10**(23), 2687–90 (2000)
10. S.J. Stray, J.M. Johnson, B.G. Kopek, A. Zlotnick, An in vitro fluorescence screen to identify antivirals that disrupt hepatitis B virus capsid assembly. Nat. Biotechnol. **24**(3), 358–362 (2006)
11. S. Thenin-Houssier, I.M. Vera, L. Pedro-Rosa, A. Brady, A. Richard, B. Konnick, S. Opp, C. Buffone, J. Fuhrmann, S. Kota, B. Billack, M. Pietka-Ottlik, T. Tellinghuisen, H. Choe, T. Spicer, L. Scampavia, F. Diaz-Griffero, D.J. Kojetin, S.T. Valente, Ebselen, a small-molecule capsid inhibitor of hiv-1 replication. Antimicrob. Agents Chemother. **60**(4), 2195–208 (2016). https://doi.org/10.1128/AAC.02574-15
12. O. Weber, K.H. Schlemmer, E. Hartmann, I. Hagelschuer, A. Paessens, E. Graef, K. Deres, S. Goldmann, U. Niewoehner, J. Stoltefuss, D. Haebich, H. Ruebsamen-Waigmann, S. Wohlfeil, Inhibition of human hepatitis b virus (hbv) by a novel non-nucleosidic compound in a transgenic mouse model. Antiviral Res. **54**(2), 69–78 (2002)
13. S.J. Stray, C.R. Bourne, S. Punna, W.G. Lewis, M.G. Finn, A. Zlotnick, A Heteroaryldihydropyrimidine sctivates and can misdirect hepatitis B virus capsid assembly. Proc. Natl. Acad. Sci. USA **102**(23), 8138–8143 (2005)
14. J.B. Bale, S. Gonen, Y. Liu, W. Sheffler, D. Ellis, C. Thomas, D. Cascio, T.O. Yeates, T. Gonen, N.P. King, D. Baker, Accurate design of megadalton-scale two-component icosahedral protein complexes. Science **353**(6297), 389–94 (2016). https://doi.org/10.1126/science.aaf8818
15. G.L. Butterfield, M.J. Lajoie, H.H. Gustafson, D.L. Sellers, U. Nattermann, D. Ellis, J.B. Bale, S. Ke, G.H. Lenz, A. Yehdego, R. Ravichandran, S.H. Pun, N.P. King, D. Baker, Evolution of a designed protein assembly encapsulating its own RNA genome. Nature **552**(7685), 415–420 (2017). https://doi.org/10.1038/nature25157
16. N.P. King, J.B. Bale, W. Sheffler, D.E. McNamara, S. Gonen, T. Gonen, T.O. Yeates, D. Baker, Accurate design of co-assembling multi-component protein nanomaterials. Nature **510**(7503), 103–8 (2014). https://doi.org/10.1038/nature13404
17. Y.T. Lai, E. Reading, G.L. Hura, K.L. Tsai, A. Laganowsky, F.J. Asturias, J.A. Tainer, C.V. Robinson, T.O. Yeates, Structure of a designed protein cage that self-assembles into a highly porous cube. Nat. Chem. **6**(12), 1065–71 (2014). https://doi.org/10.1038/nchem.2107
18. M. Mosayebi, D.K. Shoemark, J.M. Fletcher, R.B. Sessions, N. Linden, D.N. Woolfson, T.B. Liverpool, Beyond icosahedral symmetry in packings of proteins in spherical shells. Proc. Natl. Acad. Sci. **114**(34), 9014–9019 (2017). https://doi.org/10.1073/pnas.1706825114
19. C. Sigl, E.M. Willner, W. Engelen, J.A. Kretzmann, K., Sachenbacher, A. Liedl, F. Kolbe, F. Wilsch, S.A. Aghvami, U. Protzer, et al.: Programmable icosahedral shell system for virus trapping. Nat. Mater., 1–9 (2021)
20. R. Divine, V. Dang Ha, G. Ueda, A. Fallas Jorge, I. Vulovic, W. Sheffler, S. Saini, T. Zhao Yan, X. Raj Infencia, A. Morawski Peter, F. Jennewein Madeleine, J. Homad Leah, Y.-H. Wan, R. Tooley Marti, F. Seeger, A. Etemadi, L. Fahning Mitchell, J. Lazarovits, A. Roederer, C. Walls Alexandra, L. Stewart, M. Mazloomi, P. King Neil, J. Campbell Daniel, T.

McGuire Andrew, L. Stamatatos, H. Ruohola-Baker, J. Mathieu, D. Veesler, D. Baker, Designed proteins assemble antibodies into modular nanocages. Science **372**(6537), 9994 (2021). https://doi.org/10.1126/science.abd9994
21. Y. Hsia, R. Mout, W. Sheffler, N.I. Edman, I. Vulovic, Y.-J. Park, R.L. Redler, M.J. Bick, A.K. Bera, A. Courbet, A. Kang, T.J. Brunette, U. Nattermann, E. Tsai, A. Saleem, C.M. Chow, D. Ekiert, G. Bhabha, D. Veesler, D. Baker, Design of multi-scale protein complexes by hierarchical building block fusion. Nat. Commun. **12**(1), 2294 (2021). https://doi.org/10.1038/s41467-021-22276-z
22. J. Laniado, K.A. Cannon, J.E. Miller, M.R. Sawaya, D.E. McNamara, T.O. Yeates, Geometric lessons and design strategies for nanoscale protein cages. ACS Nano **15**(3), 4277–4286 (2021). https://doi.org/10.1021/acsnano.0c07167
23. S.A. McConnell, K.A. Cannon, C. Morgan, R. McAllister, B.R. Amer, R.T. Clubb, T.O. Yeates, Designed protein cages as scaffolds for building multienzyme materials. ACS Synth. Biol. **9**(2), 381–391 (2020). https://doi.org/10.1021/acssynbio.9b00407
24. A. Zlotnick, To build a virus capsid; an equilibrium-model of the self-assembly of polyhedral protein complexes. J. Mol. Biol. **241**(1), 59–67 (1994)
25. A. Zlotnick, Distinguishing reversible from irreversible virus capsid assembly. J. Mol. Biol. **366**(1), 14–18 (2007)
26. A. Zlotnick, S.J. Stray, How does your virus grow? Understanding and interfering with virus assembly. Trends Biotechnol. **21**(12), 536–542 (2003)
27. M.G. Mateu, Assembly, stability and dynamics of virus capsids. Arch. Biochem. Biophys. **531**(1–2), 65–79 (2013). https://doi.org/10.1016/j.abb.2012.10.015
28. J.D. Perlmutter, M.F. Hagan, Mechanisms of virus assembly. Annu. Rev. Phys. Chem. **66**(1), 217–239 (2015). https://doi.org/10.1146/annurev-physchem-040214-121637
29. M.F. Hagan, Modeling viral capsid assembly. Adv. Chem. Phys. **155**, 1–68 (2014)
30. R. Zandi, B. Dragnea, A. Travesset, R. Podgornik, *On virus growth and form* (Phys. Rep. 2020)
31. P.E. Prevelige, D. Thomas, J. King, Nucleation and growth phases in the polymerization of coat and scaffolding subunits into icosahedral procapsid shells. Biophys. J . **64**(3), 824–835 (1993)
32. R. Tuma, H. Tsuruta, K.H. French, P.E. Prevelige, Detection of intermediates and kinetic control during assembly of bacteriophage P22 procapsid. J. Mol. Biol. **381**(5), 1395–1406 (2008)
33. R. Twarock, R.J. Bingham, E.C. Dykeman, P.G. Stockley, A modelling paradigm for rna virus assembly. Curr. Opin. Vir. **31**, 74–81 (2018)
34. J.E. Baschek, H.C.R. Klein, U.S. Schwarz, Stochastic dynamics of virus capsid formation: direct versus hierarchical self-assembly. Bmc Biophys. **5** (2012) https://doi.org/10.1186/2046-1682-5-22
35. M.A. Boettcher, H.C.R. Klein, U.S. Schwarz, Role of dynamic capsomere supply for viral capsid self-assembly. Phys. Biol. **12**(1) (2015) https://doi.org/10.1088/1478-3975/12/1/016014
36. H.C.R. Klein, U.S. Schwarz, Studying protein assembly with reversible brownian dynamics of patchy particles. J. Chem. Phys. **140**(18) (2014) https://doi.org/10.1063/1.4873708 . Klein, Heinrich C. R. Schwarz, Ulrich S. Schwarz, Ulrich/K-4111-2014 Schwarz, Ulrich/0000-0003-1483-640X 1089-7690
37. M.S. Kumar, R. Schwartz, A parameter estimation technique for stochastic self-assembly systems and its application to human papillomavirus self-assembly. Phys. Biol. **7**(4), 045005 (2010)
38. A.J. Pak, J.M.A. Grime, P. Sengupta, A.K. Chen, A.E.P. Durumeric, A. Srivastava, M. Yeager, J.A.G. Briggs, J. Lippincott-Schwartz, G.A. Voth, Immature hiv-1 lattice assembly dynamics are regulated by scaffolding from nucleic acid and the plasma membrane. Proc. Natl. Acad. Sci. USA (2017). https://doi.org/10.1073/pnas.1706600114
39. R. Schwartz, P.W. Shor, P.E. Prevelige, B. Berger, Local rules simulation of the kinetics of virus capsid self-assembly. Biophys. J . **75**(6), 2626–2636 (1998)
40. B. Sweeney, T. Zhang, R. Schwartz, Exploring the parameter space of complex self-assembly through virus capsid models. Biophys. J . **94**(3), 772–783 (2008)
41. T.Q. Zhang, R. Schwartz, Simulation study of the contribution of oligomer/oligomer binding to capsid assembly kinetics. Biophys. J . **90**(1), 57–64 (2006)
42. A. Tan, A.J. Pak, D.R. Morado, G.A. Voth, J.A.G. Briggs, Immature hiv-1 assembles from gag dimers leaving partial hexamers at lattice edges as potential substrates for proteolytic maturation. Proc. Natl. Acad. Sci. USA **118**(3) (2021) https://doi.org/10.1073/pnas.2020054118
43. A. Yu, A.J. Pak, P. He, V. Monje-Galvan, L. Casalino, Z. Gaieb, A.C. Dommer, R.E. Amaro, G.A. Voth, A multiscale coarse-grained model of the sars-cov-2 virion. Biophys. J . **120**(6), 1097–1104 (2021)
44. M. Gupta, A.J. Pak, G.A. Voth, Critical mechanistic features of hiv-1 viral capsid assembly. Sci Adv 9(1), 7434 (2023) https://doi.org/10.1126/sciadv.add7434 . 2375–2548. Gupta, Manish Orcid: 0000-0001-6879-0617 Pak, Alexander J Orcid: 0000-0003-2823-6480 Voth, Gregory A Orcid: 0000-0002-3267-6748 F32 AI150477/AI/NIAID NIH HHS/United States R01 AI150492/AI/NIAID NIH HHS/United States U54 AI170855/AI/NIAID NIH HHS/United States Journal Article United States 2023/01/07 Sci Adv. 2023;9(1):eadd7434. https://doi.org/10.1126/sciadv.add7434. Epub 2023 Jan 6
45. S. Panahandeh, S. Li, L. Marichal, R. Leite Rubim, G. Tresset, R. Zandi, How a virus circumvents energy barriers to form symmetric shells. ACS Nano **14**(3), 3170–3180 (2020). https://doi.org/10.1021/acsnano.9b08354
46. M.F. Hagan, D. Chandler, Dynamic pathways for viral capsid assembly. Biophys. J . **91**(1), 42–54 (2006)
47. R.L. Jack, M.F. Hagan, D. Chandler, Fluctuation-dissipation ratios in the dynamics of self-assembly. Phys. Rev. E **76**, 021119 (2007)
48. D.C. Rapaport, The role of reversibility in viral capsid growth: a paradigm for self-assembly. Phys. Rev. Lett. **101**, 186101 (2008)
49. S. Whitelam, C. Rogers, A. Pasqua, C. Paavola, J. Trent, P.L. Geissler, The impact of conformational fluctuations on self-assembly: cooperative aggregation of

archaeal chaperonin proteins. Nano Lett. **9**, 292–297 (2009)
50. H.D. Nguyen, V.S. Reddy, C.L. Brooks, Deciphering the kinetic mechanism of spontaneous self-assembly of icosahedral capsids. Nano Lett. **7**(2), 338–344 (2007)
51. A.W. Wilber, J.P.K. Doye, A.A. Louis, E.G. Noya, M.A. Miller, P. Wong, Reversible self-assembly of patchy particles into monodisperse icosahedral clusters. J. Chem. Phys. **127**(8), 085106 (2007)
52. A.W. Wilber, J.P.K. Doye, A.A. Louis, A.C.F. Lewis, Monodisperse self-assembly in a model with protein-like interactions. J. Chem. Phys. **131**(17), 175102 (2009)
53. M.F. Hagan, O.M. Elrad, R.L. Jack, Mechanisms of kinetic trapping in self-assembly and phase transformation. J. Chem. Phys. **135**, 104115 (2011)
54. S. Cheng, A. Aggarwal, M.J. Stevens, Self-assembly of artificial microtubules. Soft Matter 8(20), 5666 (2012). https://doi.org/10.1039/c2sm25068c. arXiv:1201.2328v1
55. G.R. Lázaro, S. Mukhopadhyay, M.F. Hagan, Why enveloped viruses need cores: the contribution of a nucleocapsid core to viral budding. Biophys. J . **114**(3), 619–630 (2018). https://doi.org/10.1016/j.bpj.2017.11.3782
56. T. Chen, S.C. Glotzer, Simulation studies of a phenomenological model for elongated virus capsid formation. Phys. Rev. E **75**, 051504 (2007)
57. R.F. Bruinsma, W.M. Gelbart, D. Reguera, J. Rudnick, R. Zandi, Viral self-assembly as a thermodynamic process. Phys. Rev. Lett. **90**(24), 248101 (2003)
58. R. Zandi, D. Reguera, R.F. Bruinsma, W.M. Gelbart, J. Rudnick, Origin of icosahedral symmetry in viruses. Proc. Natl. Acad. Sci. USA **101**(44), 15556–15560 (2004)
59. B. Berger, P.W. Shor, L. Tuckerkellogg, J. King, Local rule-based theory of virus shell assembly. Proc. Natl. Acad. Sci. USA **91**(16), 7732–7736 (1994)
60. R. Schwartz, R.L. Garcea, B. Berger, "Local rules" theory applied to polyomavirus polymorphic capsid assemblies. Virology **268**(2), 461–470 (2000)
61. D.C. Rapaport, Self-assembly of polyhedral shells: a molecular dynamics study. Phys. Rev. E **70**, 051905 (2004)
62. H.D. Nguyen, V.S. Reddy, C.L. Brooks, Invariant polymorphism in virus capsid assembly. J. Am. Chem. Soc. **131**(7), 2606–14 (2009)
63. O.M. Elrad, M.F. Hagan, Mechanisms of size control and polymorphism in viral capsid assembly. Nano Lett. **8**(11), 3850–3857 (2008)
64. I.G. Johnston, A.A. Louis, J.P.K. Doye, Modelling the self-assembly of virus capsids. J. Phys.: Condens. Matter **22**(10), 104101 (2010)
65. D.C. Rapaport, Studies of reversible capsid shell growth. J. Phys.: Condens. Matter **22**(10), 104115 (2010)
66. H. Nguyen, C. Brooks, Generalized structural polymorphism in self-assembled viral particles. Nano Lett. **8**, 4574 (2008)
67. R.F. Bruinsma, W.S. Klug, Physics of viral shells. Annu. Rev. Condens. Matter Phys. **6**(1), 245–268 (2015). https://doi.org/10.1146/annurev-conmatphys-031214-014325
68. M.F. Hagan, R. Zandi, Recent advances in coarse-grained modeling of virus assembly. Curr. Opin. Vir. **18**, 36 (2016)
69. D.C. Rapaport, Molecular dynamics simulation of reversibly self-assembling shells in solution using trapezoidal particles. Phys. Rev. E **86**, 051917 (2012) https://doi.org/10.1103/PhysRevE.86.051917
70. D.C. Rapaport, J.E. Johnson, J. Skolnick, Supramolecular self-assembly: molecular dynamics modeling of polyhedral shell formation. Comput. Phys. Commun. **122**, 231–235 (1999)
71. C.I. Mendoza, D. Reguera, Shape selection and misassembly in viral capsid formation by elastic frustration. eLife **9**, 52525 (2020)
72. J. Wagner, R. Zandi, The robust assembly of small symmetric nanoshells. Biophys. J . **109**, 956 (2015)
73. M. Castelnovo, T. Verdier, L. Foret, Comparing open and closed molecular self-assembly. Epleurophys. Lett. **105**(2) (2014) https://doi.org/10.1209/0295-5075/105/28006
74. M. Castelnovo, D. Muriaux, C. Faivre-Moskalenko, Entropic control of particle sizes during viral self-assembly. New J. Phys. **15** (2013) https://doi.org/10.1088/1367-2630/15/3/035028
75. R. Zandi, P. Schoot, D. Reguera, W. Kegel, H. Reiss, Classical nucleation theory of virus capsids. Biophys. J . **90**(6), 1939–1948 (2006)
76. P. Schoot, R. Zandi, Kinetic theory of virus capsid assembly. Phys. Biol. **4**(4), 296–304 (2007)
77. L. Lavelle, M. Gingery, M. Phillips, W.M. Gelbart, C.M. Knobler, R.D. Cadena-Nava, J.R. Vega-Acosta, L.A. Pinedo-Torres, J. Ruiz-Garcia, Phase diagram of self-assembled viral capsid protein polymorphs. J. Phys. Chem. B **113**(12), 3813–3819 (2009)
78. K. Zhou, L. Li, Z. Tan, A. Zlotnick, S.C. Jacobson, Characterization of hepatitis B virus capsids by resistive-pulse sensing. J. Am. Chem. Soc. **133**(6), 1618–1621 (2011)
79. J. Zhou, P. Kondylis, D.G. Haywood, Z.D. Harms, L.S. Lee, A. Zlotnick, S.C. Jacobson, Characterization of virus capsids and their assembly intermediates by multicycle resistive-pulse sensing with four pores in series. Anal. Chem. **90**(12), 7267–7274 (2018). https://doi.org/10.1021/acs.analchem.8b00452
80. C. Uetrecht, I.M. Barbu, G.K. Shoemaker, E. Duijn, J.R. Heck Albert, Interrogating viral capsid assembly with ion mobility-mass spectrometry. Nat. Chem. **3**(2), 126–132 (2011)
81. E.E. Pierson, D.Z. Keifer, L. Selzer, L.S. Lee, N.C. Contino, J.C.-Y. Wang, A. Zlotnick, M.F. Jarrold, Detection of late intermediates in virus capsid assembly by charge detection mass spectrometry. J. Am. Chem. Soc. **136**(9), 3536–3541 (2014)
82. E.E. Pierson, D.Z. Keifer, A.A. Kukreja, J.C.-Y. Wang, A. Zlotnick, M.F. Jarrold, Charge detection mass spectrometry identifies preferred non-icosahedral polymorphs in the self-assembly of woodchuck hepatitis virus capsids. J. Mol. Biol. **428**(2), 292–300 (2016)
83. C. Lutomski, N.A. Lyktey, E.E. Pierson, Z. Zhao, A. Zlotnick, M.F. Jarrold, Multiple pathways in capsid assembly. J. Am. Chem. Soc. **140**(17), 5784–5790 (2018). https://doi.org/10.1021/jacs.8b01804

84. A.R. Todd, L.F. Barnes, K. Young, A. Zlotnick, M.F. Jarrold, Higher resolution charge detection mass spectrometry. Anal. Chem. **92**(16), 11357–11364 (2020). https://doi.org/10.1021/acs.analchem.0c02133
85. P. Buzon, S. Maity, P. Christodoulis, M.J. Wiertsema, S. Dunkelbarger, C. Kim, G.J. Wuite, A. Zlotnick, W.H. Roos, Virus self-assembly proceeds through contact-rich energy minima. Sci. Adv. **7**(45), 0811 (2021)
86. R. Asor, C.J. Schlicksup, Z. Zhao, A. Zlotnick, U. Raviv, Rapidly forming early intermediate structures dictate the pathway of capsid assembly. J. Am. Chem. Soc. **142**(17), 7868–7882 (2020)
87. M. Chevreuil, L. Lecoq, S. Wang, L. Gargowitsch, N. Nhiri, E. Jacquet, T. Zinn, S. Fieulaine, S. Bressanelli, G. Tresset, Nonsymmetrical dynamics of the HBV capsid assembly and disassembly evidenced by their transient species. J. Phys. Chem. B **124**(45), 9987–9995 (2020). https://doi.org/10.1021/acs.jpcb.0c05024
88. G. Tresset, C. Le Coeur, J.-F. Bryche, M. Tatou, M. Zeghal, A. Charpilienne, D. Poncet, D. Constantin, S. Bressanelli, Norovirus capsid proteins self-assemble through biphasic kinetics via long-lived stave-like intermediates. J. Am. Chem. Soc. **135**(41), 15373–15381 (2013)
89. M. Chevreuil, D. Law-Hine, J. Chen, S. Bressanelli, S. Combet, D. Constantin, J. Degrouard, J. Möller, M. Zeghal, G. Tresset, Nonequilibrium self-assembly dynamics of icosahedral viral capsids packaging genome or polyelectrolyte. Nat. Commun. **9**(1), 3071 (2018)
90. S. Kler, J.C.-Y. Wang, M. Dhason, A. Oppenheim, A. Zlotnick, Scaffold properties are a key determinant of the size and shape of self-assembled virus-derived particles. ACS Chem. Biol. **8**(12), 2753–61 (2013). https://doi.org/10.1021/cb4005518
91. S. Kler, R. Asor, C. Li, A. Ginsburg, D. Harries, A. Oppenheim, A. Zlotnick, U. Raviv, RNA encapsidation by SV40-derived nanoparticles follows a rapid two-state mechanism. J. Am. Chem. Soc. **134**(21), 8823–8830 (2012)
92. R. Asor, C.J. Schlicksup, Z. Zhao, A. Zlotnick, U. Raviv, Rapidly forming early intermediate structures dictate the pathway of capsid assembly. J. Am. Chem. Soc. **142**(17), 7868–7882 (2020). https://doi.org/10.1021/jacs.0c01092. (**PMID: 32233479**)
93. R. Asor, L. Selzer, C.J. Schlicksup, Z. Zhao, A. Zlotnick, U. Raviv, Assembly reactions of hepatitis b capsid protein into capsid nanoparticles follow a narrow path through a complex reaction landscape. ACS Nano **13**(7), 7610–7626 (2019)
94. R.D. Cadena-Nava, M. Comas-Garcia, R.F. Garmann, A.L.N. Rao, C.M. Knobler, W.M. Gelbart, Self-assembly of viral capsid protein and RNA molecules of different sizes: requirement for a specific high protein/RNA mass ratio. J. Virol. **86**(6), 3318–3326 (2012)
95. M. Comas-Garcia, R.D. Cadena-Nava, A.L.N. Rao, C.M. Knobler, W.M. Gelbart, In vitro quantification of the relative packaging efficiencies of single-stranded RNA molecules by viral capsid protein. J. Virol. **86**(22), 12271–12282 (2012)
96. R.F. Garmann, M. Comas-Garcia, M.S.T. Koay, J.J.L.M. Cornelissen, C.M. Knobler, W.M. Gelbart, The role of electrostatics in the assembly pathway of a single-stranded RNA virus. J. Virol. (2014). https://doi.org/10.1128/jvi.01044-14
97. Y. Hu, R. Zandi, A. Anavitarte, C.M. Knobler, W.M. Gelbart, Packaging of a polymer by a viral capsid: the interplay between polymer length and capsid size. Biophys. J . **94**(4), 1428–1436 (2008)
98. S.N. Fejer, D. Chakrabarti, D.J. Wales, Emergent complexity from simple anisotropic building blocks: shells, tubes, and spirals. ACS Nano **4**(1), 219–228 (2010)
99. R. Kusters, H.-K. Lin, R. Zandi, I. Tsvetkova, B. Dragnea, P. Schoot, Role of charge regulation and size polydispersity in nanoparticle encapsulation by viral coat proteins. J. Phys. Chem. B **119**(5), 1869–1880 (2015). https://doi.org/10.1021/jp5108125
100. R. Zandi, P. Schoot, Size regulation of ss-RNA viruses. Biophys. J . **96**(1), 9–20 (2009)
101. M.F. Hagan, Controlling viral capsid assembly with templating. Phys. Rev. E **77**, 051904 (2008)
102. M.F. Hagan, A theory for viral capsid assembly around electrostatic cores. J. Chem. Phys. **130**, 114902 (2009)
103. V.A. Belyi, M. Muthukumar, Electrostatic origin of the genome packing in viruses. Proc. Natl. Acad. Sci. USA **103**(46), 17174–17178 (2006)
104. R. Twarock, R.J. Bingham, E.C. Dykeman, P.G. Stockley, A modelling paradigm for rna virus assembly. Curr. Opin. Vir. **31**, 74–81 (2018)
105. S. Li, P. Roy, A. Travesset, R. Zandi, Why large icosahedral viruses need scaffolding proteins. Proc. Natl. Acad. Sci. USA **115**(43), 10971–10976 (2018)
106. S. Li, R. Zandi, A. Travesset, G.M. Grason, Ground states of crystalline caps: generalized jellium on curved space. Phys. Rev. Lett. (2019). https://doi.org/10.1103/PhysRevLett.123.145501. arXiv:1906.03301
107. P. Schoot, R. Zandi, Impact of the topology of viral rnas on their encapsulation by virus coat proteins. J. Biol. Phys. **39**(2), 289–299 (2013). https://doi.org/10.1007/s10867-013-9307-y
108. G. Erdemci-Tandogan, J. Wagner, P. Schoot, R. Podgornik, R. Zandi, RNA topology remolds electrostatic stabilization of viruses. Phys. Rev. E **89**, 032707 (2014) https://doi.org/10.1103/PhysRevE.89.032707
109. A. Siber, R. Zandi, R. Podgornik, Thermodynamics of nanospheres encapsulated in virus capsids. Phys. Rev. E **81**(5), 051919 (2010)
110. E.C. Dykeman, P.G. Stockley, R. Twarock, Packaging signals in two single-stranded RNA viruses imply a conserved assembly mechanism and geometry of the packaged genome. J. Mol. Biol. **425**(17), 3235–49 (2013). https://doi.org/10.1016/j.jmb.2013.06.005
111. N. Patel, E.C. Dykeman, R.H.A. Coutts, G.P. Lomonossoff, D.J. Rowlands, S.E.V. Phillips, N. Ranson, R. Twarock, R. Tuma, P.G. Stockley, Revealing the density of encoded functions in a viral rna. Proc. Natl. Acad. Sci. USA (2015). https://doi.org/10.1073/pnas.1420812112
112. E.C. Dykeman, P.G. Stockley, R. Twarock, Solving a Levinthal's paradox for virus assembly identifies a unique antiviral strategy. Proc. Natl. Acad. Sci. USA **111**(14), 5361–5366 (2014). https://doi.org/10.1073/pnas.1319479111
113. E.C. Dykeman, P.G. Stockley, R. Twarock, Building a viral capsid in the presence of genomic RNA. Phys.

Rev. E **87**(2), 022717 (2013). https://doi.org/10.1103/PhysRevE.87.022717
114. V.L. Morton, E.C. Dykeman, N.J. Stonehouse, A.E. Ashcroft, R. Twarock, P.G. Stockley, The impact of viral RNA on assembly pathway selection. J. Mol. Biol. **401**(2), 298–308 (2010)
115. R. Zhang, E. Wernersson, P. Linse, Icosahedral capsid formation by capsomer subunits and a semiflexible polyion. RSC Adv. **3**(47), 25258–25267 (2013). https://doi.org/10.1039/c3ra44533j
116. R. Zhang, P. Linse, Topological effects on capsomer-polyion co-assembly. J. Chem. Phys. **140**(24) (2014) https://doi.org/10.1063/1.4883056
117. R. Zhang, P. Linse, Icosahedral capsid formation by capsomers and short polyions. J. Chem. Phys. **138**(15) (2013) https://doi.org/10.1063/1.4799243
118. D.G. Angelescu, J. Stenhammar, P. Linse, Packaging of a flexible polyelectrolyte inside a viral capsid: effect of salt concentration and salt valence. J. Phys. Chem. B **111**(29), 8477–8485 (2007)
119. D.G. Angelescu, P. Linse, Monte Carlo simulations of flexible polyelectrolytes inside viral capsids with dodecahedral charge distribution. Phys. Rev. E **75**(5 Pt 1), 051905 (2007)
120. S. Panahandeh, S. Li, R. Zandi, The equilibrium structure of self-assembled protein nano-cages. Nanoscale **10**, 22802–22809 (2018) https://doi.org/10.1039/C8NR07202G
121. C. Waltmann, R. Asor, U. Raviv, M. Cruz, Assembly and stability of simian virus 40 polymorphs. ACS Nano **14**(4), 4430–4443 (2020). https://doi.org/10.1021/acsnano.9b10004. (**PMID: 32208635**)
122. J.D. Perlmutter, C. Qiao, M.F. Hagan, Viral genome structures are optimal for capsid assembly. eLife **2**, 00632 (2013)
123. J.D. Perlmutter, M.R. Perkett, M.F. Hagan, Pathways for virus assembly around nucleic acids. J. Mol. Biol. (2014). https://doi.org/10.1016/j.jmb.2014.07.004
124. A. Ginsburg, T. Ben-Nun, R. Asor, A. Shemesh, L. Fink, R. Tekoah, Y. Levartovsky, D. Khaykelson, R. Dharan, A. Fellig, U. Raviv, D+: Software for High-Resolution Hierarchical Modeling of Solution X-Ray Scattering from Complex Structures. J. Appl. Crystallogr. **52**, 219–242 (2019) https://doi.org/10.1107/S1600576718018046
125. A. Ginsburg, T. Ben-Nun, R. Asor, A. Shemesh, I. Ringel, U. Raviv, Reciprocal grids: a hierarchical algorithm for computing solution x-ray scattering curves from supramolecular complexes at high resolution. J. Chem. Inf. Model. **56**(8) (2016) https://doi.org/10.1021/acs.jcim.6b00159
126. R. Asor, O. Ben-nun-Shaul, A. Oppenheim, U. Raviv, Crystallization, reentrant melting, and resolubilization of virus nanoparticles. ACS Nano **11**(10), 9814–9824 (2017)
127. A. Ginsburg, A. Shemesh, A. Millgram, R. Dharan, Y. Levi-Kalisman, I. Ringel, U. Raviv, Structure of dynamic, taxol-stabilized, and gmppcp-stabilized microtubule. J. Phys. Chem. B **121**(36), 8427–8436 (2017)
128. H. Fischer, M.d. Oliveira Neto, H. Napolitano, I. Polikarpov, A.F. Craievich, Determination of the molecular weight of proteins in solution from a single small-angle x-ray scattering measurement on a relative scale. J. Appl. Crystallogr. **43**(1), 101–109 (2010)
129. T. Ben-Nun, A. Ginsburg, P. Székely, U. Raviv, X+: a comprehensive computationally accelerated structure analysis tool for solution x-ray scattering from supramolecular self-assemblies. J. Appl. Crystallogr. **43**(6), 1522–1531 (2010). https://doi.org/10.1107/S0021889810032772
130. P. Székely, A. Ginsburg, T. Ben-Nun, U. Raviv, Solution x-ray scattering form factors of supramolecular self-assembled structures. Langmuir **26**(16), 13110–13129 (2010)
131. R.P. Rambo, J.A. Tainer, Characterizing flexible and intrinsically unstructured biological macromolecules by sas using the porod-debye law. Biopolymers **95**(8), 559–571 (2011)
132. S. Ciccariello, J. Goodisman, H. Brumberger, On the porod law. J. Appl. Crystallogr. **21**(2), 117–128 (1988)
133. P. Schoot, R. Bruinsma, Electrostatics and the assembly of an rna virus. Phys. Rev. E **71**(6), 061928 (2005)
134. A. Zlotnick, J.M. Johnson, P.W. Wingfield, S.J. Stahl, D. Endres, A theoretical model successfully identifies features of hepatitis B virus capsid assembly. Biochemistry **38**(44), 14644–14652 (1999)
135. A. Zlotnick, P. Ceres, S. Singh, J.M. Johnson, A small molecule inhibits and misdirects assembly of hepatitis b virus capsids. J. Virol. **76**(10), 4848–4854 (2002)
136. A. Zlotnick, Are weak protein–protein interactions the general rule in capsid assembly? Virology **315**, 269–274 (2003)
137. P. Ceres, A. Zlotnick, Weak protein–protein interactions are sufficient to drive assembly of hepatitis B virus capsids. Biochemistry **41**(39), 11525–11531 (2002)
138. S. Mukherjee, M. Abd-El-Latif, M. Bronstein, O. Bennun-Shaul, S. Kler, A. Oppenheim, High cooperativity of the sv40 major capsid protein vp1 in virus assembly. PLoS ONE **2**(8), 765 (2007)
139. C.E. Blanchet, A. Spilotros, F. Schwemmer, M.A. Graewert, A. Kikhney, C.M. Jeffries, D. Franke, D. Mark, R. Zengerle, F. Cipriani, S. Fiedler, M. Roessle, D.I. Svergun, Versatile sample environments and automation for biological solution X-ray scattering experiments at the p12 beamline (petra iii, desy). J. Appl. Crystallogr. **48**(2), 431–443 (2015). https://doi.org/10.1107/S160057671500254X
140. A. Round, F. Felisaz, L. Fodinger, A. Gobbo, J. Huet, C. Villard, C.E. Blanchet, P. Pernot, S. McSweeney, M. Roessle, D.I. Svergun, F. Cipriani, Biosaxs sample changer: a robotic sample changer for rapid and reliable high-throughput x-ray solution scattering experiments. Acta Crystallogr. Sect. D **71**(1), 67–75 (2015). https://doi.org/10.1107/S1399004714026959
141. D. Franke, A.G. Kikhney, D.I. Svergun, Automated acquisition and analysis of small angle x-ray scattering data. Nucl. Instrum. Methods Phys. Res., Sect. A **689**, 52–59 (2012)
142. P. Van Vaerenbergh, J. Léonardon, M. Sztucki, P. Boesecke, J. Gorini, L. Claustre, F. Sever, J. Morse, T. Narayanan, An upgrade beamline for combined wide, small and ultra small-angle x-ray scattering at the esrf. In: Proceedings of the 12th International Conference

on Synchrotron Radiation Instrumentation (SRI2015), vol. 1741, p. 030034 (2016). AIP Publishing
143. T. Narayanan, M. Sztucki, P. Van Vaerenbergh, J. Léonardon, J. Gorini, L. Claustre, F. Sever, J. Morse, P. Boesecke, A multipurpose instrument for time-resolved ultra-small-angle and coherent X-ray scattering. J. Appl. Crystallogr. **51**(6), 1511–1524 (2018). https://doi.org/10.1107/S1600576718012748
144. T. Narayanan, M. Sztucki, T. Zinn, J. Kieffer, A. Homs-Puron, J. Gorini, P. Van Vaerenbergh, P. Boesecke, Performance of the time-resolved ultra-small-angle X-ray scattering beamline with the Extremely Brilliant Source. J. Appl. Crystallogr. **55**(1), 98–111 (2022). https://doi.org/10.1107/S1600576721012693
145. D.J. Wales, The energy landscape as a unifying theme in molecular science. Phil. Trans. R. Soc. A **363**(1827), 357–375 (2005)
146. S.N. Fejer, T.R. James, J. Hernandez-Rojas, D.J. Wales, Energy landscapes for shells assembled from pentagonal and hexagonal pyramids. Phys. Chem. Chem. Phys. **11**(12), 2098–2104 (2009)
147. J.D. Perlmutter, M.F. Hagan, The role of packaging sites in efficient and specific virus assembly. J. Mol. Biol. (2015). https://doi.org/10.1016/j.jmb.2015.05.008
148. J.D. Perlmutter, F. Mohajerani, M.F. Hagan, Many-molecule encapsulation by an icosahedral shell. eLife **5**, 14078 (2016) https://doi.org/10.7554/eLife.14078
149. F. Mohajerani, M.F. Hagan, The role of the encapsulated cargo in microcompartment assembly. PLoS Comput. Biol. **14**(7), 1006351 (2018)
150. F. Mohajerani, E. Sayer, C. Neil, K. Inlow, M.F. Hagan, Mechanisms of scaffold-mediated microcompartment assembly and size control. ACS Nano **15**(3), 4197–4212 (2021)
151. J.A. Anderson, C.D. Lorenz, A. Travesset, General purpose molecular dynamics simulations fully implemented on graphics processing units. J. Comput. Phys. **227**(10), 5342–5359 (2008)
152. T.D. Nguyen, C.L. Phillips, J.A. Anderson, S.C. Glotzer, Rigid body constraints realized in massively-parallel molecular dynamics on graphics processing units. Comput. Phys. Commun. **182**(11), 2307–2313 (2011)
153. D.N. LeBard, B.G. Levine, P. Mertmann, S.A. Barr, A. Jusufi, S. Sanders, M.L. Klein, A.Z. Panagiotopoulos, Self-assembly of coarse-grained ionic surfactants accelerated by graphics processing units. Soft Matter **8**(8), 2385–2397 (2012)
154. T. Ben-Nun, R. Asor, A. Ginsburg, U. Raviv, Solution X-ray scattering form-factors with arbitrary electron density profiles and polydispersity distributions. Isr. J. Chem. **56**(8), 622–628 (2016). https://doi.org/10.1002/ijch.201500037
155. E. Balken, I. Ben-Nun, A. Fellig, D. Khaykelson, U. Raviv, Upgrade of D+ software for hierarchical modeling of X-ray scattering data from complex structures in solution, fibers and single orientations. J. Appl. Crystallogr. **56**(Pt 4), 1295–1303 (2023). https://doi.org/10.1107/S1600576723005319
156. U. Raviv, R. Asor, A. Shemesh, A. Ginsburg, T. Ben-Nun, Y. Schilt, Y. Levartovsky, I. Ringel, Insight into structural biophysics from solution X-ray scattering. J Struct Biol. **215**(4), 108029 (2023). https://doi.org/10.1016/j.jsb.2023.108029
157. J. MacQueen, Some methods for classification and analysis of multivariate observations. In: Proceedings of the Fifth Berkeley Symposium on Mathematical Statistics and Probability, Volume 1: Statistics, pp. 281–297. University of California Press, Berkeley, Calif. (1967). https://projecteuclid.org/euclid.bsmsp/1200512992